Article

SOURCE DATA TRANSPARENT PROCESS OPEN ACCESS CHECK FOR UPDATES

THE EMBO JOURNAL

Cyclin-dependent kinase inhibitor p18 regulates lineage transitions of excitatory neurons, astrocytes, and interneurons in the mouse cortex

Wonyoung Lee[1], Byunghee Kang[2], Hyo-Min Kim[3], Tsuyoshi Ishida[4], Minkyung Shin[1], Misato Iwashita[1], Masahiro Nitta[5], Aki Shiraishi[6], Hiroshi Kiyonari[6], Koichiro Shimoya[7], Kazuto Masamoto[5], Tae-Young Roh[8]✉ & Yoichi Kosodo[1,9]✉

Abstract

Neural stem cells (NSCs) can give rise to both neurons and glia, but the regulatory mechanisms governing their differentiation transitions remain incompletely understood. Here, we address the role of cyclin-dependent kinase inhibitors (CDKIs) in the later stages of dorsal cortical development. We find that the CDKIs p18 and p27 are upregulated at the onset of astrocyte generation. Acute manipulation of p18 and p27 levels shows that CDKIs modulate lineage switching between upper-layer neurons and astrocytes at the transitional stage. We generate a conditional knock-in mouse model to induce p18 in NSCs. The transcriptomic deconvolution of microdissected tissue reveals that increased levels of p18 promote glial cell development and activate Delta-Notch signaling. Furthermore, we show that p18 upregulates the homeobox transcription factor Dlx2 to subsequently induce the differentiation of olfactory bulb interneurons while reducing the numbers of upper-layer neurons and astrocytes at the perinatal stage. Clonal analysis using transposon-based reporters reveals that the transition from the astrocyte to the interneuron lineage is potentiated by p18 at the single-cell level. In sum, our study reports a function of p18 in determining the developmental boundaries among different cellular lineages arising sequentially from NSCs in the dorsal cortex.

Keywords Cyclin-dependent Kinase Inhibitors; Astrocyte Differentiation; Ink4 Family; Neural Stem Cells; Brain Development

Subject Categories Development; Neuroscience; Stem Cells & Regenerative Medicine

https://doi.org/10.1038/s44318-024-00325-9

Received 30 July 2024; Revised 13 November 2024; Accepted 14 November 2024

Published online: 12 December 2024

Introduction

One of the astonishing abilities of neural stem cells (NSCs) is that they can differentiate into several subtypes of neurons and macroglial cells, namely, astrocytes and oligodendrocytes, in the developing brain. Fate choice between neuron and glial cells is critical to determining brain structure, function, and evolution. In the neocortex, the production of neurons and glial cells sequentially takes place along the developmental timing (Kriegstein and Alvarez-Buylla, 2009; Taverna et al, 2014). Initially, neurons are produced directly from apical progenitors (neuroepithelial and radial glial cells (RGCs)), the subtypes of NSCs located in the ventricular zone (VZ) maintaining the apical membrane and junctional complex, or via basally located intermediate progenitors. Subsequently, apical progenitors start to produce astrocytes and then oligodendrocytes. Therefore, it is assumed that there is a switching mechanism from neuron to glial production in the differentiation program of NSCs. Indeed, previous studies have proposed that several pathways are involved in switching NSC progenies from neural to glial cells. Toward astrocytic differentiation, in particular, the roles of signaling pathways (gp130/JAK/STAT (Nakashima et al, 1999), MEK/MAPK (Li et al, 2012), and FGF (Dinh Duong et al, 2019)), transcription factors (Sox9 (Kang et al, 2012) and Zbtb20 (Nagao et al, 2016)), and epigenetic regulation (Nakagawa et al, 2020; Tiwari et al, 2018) are considered to have significant contributions.

Another possible prominent factor in deciding the cell fate of NSCs is the length of the cell cycle (Dalton, 2015; Dehay and Kennedy, 2007; Salomoni and Calegari, 2010). It has been well illustrated that the cell cycle length of the apical progenitor, particularly the G1 phase, is prolonged along stages of neural differentiation during brain development (Caviness et al, 1999; Hindley and Philpott, 2012). The length of each cell cycle phase is coordinated by cyclins, cyclin-dependent kinases (CDKs), and their inhibitors (CDKIs). In total, 8 CDKIs exist in the mouse and

---

[1]Neural Regeneration Lab, Neural Circuit Research Group, Korea Brain Research Institute, Daegu, Republic of Korea. [2]Department of Life Sciences, Pohang University of Science and Technology, Pohang, Republic of Korea. [3]College of Pharmacy, Ewha Womans University, Seoul, Republic of Korea. [4]Department of Obstetrics and Gynecology, Kobe Tokushukai Hospital, Kobe, Japan. [5]Center for Neuroscience and Biomedical Engineering, The University of Electro-Communications, Tokyo, Japan. [6]Laboratory for Animal Resources and Genetic Engineering, RIKEN Center for Biosystems Dynamics Research, Kobe, Japan. [7]Department of Obstetrics and Gynecology, Kawasaki Medical School, Kurashiki, Japan. [8]Department of Life Sciences, Ewha Womans University, Seoul, Republic of Korea. [9]Department of Brain Sciences, Daegu Gyeongbuk Institute of Science and Technology, Daegu, Republic of Korea. ✉E-mail: tyroh@ewha.ac.kr; kosodo@kbri.re.kr

human genomes. While Cdkn3 is expressed mostly in cancer (Nalepa et al, 2013), other CDKIs are categorized into the Cip/Kip family (p21 encoded by *cdkn1a*, p27/*cdkn1b*, and p57/*cdkn1c*) and INK4 family (p16/*cdkn2a*, p15/*cdkn2b*, p18/*cdkn2c*, and p19/*cdkn2d*) (Besson et al, 2008). Among Cip/Kip family members, p27 and p57 are known to regulate several events in neural differentiation, for instance, enhancing neurogenesis and neural migration (Itoh et al, 2007; Mairet-Coello et al, 2012; Nguyen et al, 2006) as well as NSC quiescence in the adult brain (Andreu et al, 2015; Caron et al, 2018; Furutachi et al, 2013). It has also been reported that p57 determines the origin of adult NSCs at the lateral ganglionic eminence (GE) (Furutachi et al, 2015; Harada et al, 2021). In contrast to the intensive analyses of p27 and p57 in the neurogenic phase, their roles in gliogenesis remain elusive. An earlier work by Tury et al described that the overexpression (OE) of p27 and p57 in the embryonic rat brain resulted in ectopic GFAP-positive cells in the postnatal day (P) 10 brain (Tury et al, 2011). However, to uncover the watershed between neural and glial lineages, it is essential to address whether CDKI-induced glial features appear in an immediate manner or later as an indirect consequence. Hence, multi-aspect investigations of neural and glial signatures combined with the acute manipulation of CDKIs in NSCs need to be conducted.

It should also be mentioned that, compared to that of the Cip/Kip family, the role of the INK4 family in brain development has yet to be explored (Ding et al, 2020; Grison and Atanasoski, 2020). Curiously, previous studies using knockout mice have shown that individual p27 (Fero et al, 1996; Kiyokawa et al, 1996; Nakayama et al, 1996) and p18 (Franklin et al, 1998) null mice share phenotypic similarities in the aspects of increased body size with multiple organ hyperplasia even though they belong to different subfamilies. Such a phenotype is exaggerated in p18/p27 double null mice, suggesting that p18 and p27 act in separate pathways to regulate tissue growth collaboratively (Franklin et al, 1998). On the other hand, INK4 family gene double null mice, such as p15/p18 (Latres et al, 2000) and p18/p19 (Zindy et al, 2001), exhibit only minor phenotypes at birth, indicating that they function in different cellular lineages and pathways.

Here, we investigated the role of CDKIs in the later stage of cortical development. Among CDKIs, we observed that p18 and p27 increased in apical progenitors in the VZ at the onset of gliogenesis. Manipulation of CDKI expression revealed their role in lineage switching between neurons and astrocytes. Remarkably, transcriptomic deconvolution using a conditional p18 knock-in mouse and functional molecular analysis elucidated not only the transition from neurons to astrocytes but also further lineage switching toward olfactory bulb (OB) interneurons. These results indicate that p18 integratedly determines the lineage boundaries of progeny sequentially arising from NSCs of dorsal cortical origin.

Results

Expression profiling of CDKIs in the neural and glial generation stage

To address the role of CDKIs in apical progenitors in the developing brain, we first investigated the expression levels of all CDKIs by re-examining published single-cell transcriptome data (La Manno et al, 2021). Among eight CDKIs in the mouse genome classified as *Cdkn1*, *Cdkn2*, and *Cdkn3*, *p18* and *p27* showed a peak at the onset of the gliogenesis stage (E15-16, Fig. EV1A). We then attempted immunostaining using specific antibodies against p18 and p27 (Fig. EV1B,C) to profile the spatiotemporal localization of each protein in the *AldH1l1*-EGFP mouse line, which expresses EGFP as an astrocyte-specific reporter (Fig. EV1D) (Nagao et al, 2016; Yang et al, 2011). In the E15.5 dorsal cortex, the p18 signal was recognized mainly in the VZ, where apical progenitors localize (Fig. 1A). This pattern fits well with p18 mRNA expression (Zindy et al, 1997). On the other hand, p27 was found not only in the VZ but also in the intermediate zone (IZ) and cortical plate (CP) (Fig. 1A), as previously reported (Nguyen et al, 2006). We next addressed the stage-dependent transition of p18, p27, and *AldH1l1*-EGFP signals in the VZ from E13.5 to E17.5 (Fig. 1B,C). Notably, p18 showed the highest immunofluorescent signal at E15.5, while p27 showed an increase along the stages. The *AldH1l1*-EGFP signal appeared in the VZ at E15.5, and then the expression level was sustained. To validate the result, we examined the mRNA expression levels of *p18*, *p27*, and *EGFP* in the VZ by capturing the tissue fraction using laser microdissection (LMD), followed by quantitative PCR (qPCR) of the extracted lysate (Figs. 1D and EV1E). Compared to the immunostaining results, a similar tendency was observed (Fig. 1E), verifying that specific expression patterns of p18 and p27 correlated with the initiation of astrocyte generation.

Role of CDKIs in lineage switching between neurons and astrocytes

To explore whether there is a functional link between the presence of CDKIs and neural to astrocytic differentiation switching, gene manipulation was attempted. We suppressed p18 and p27 functions using a miRNA-based knockdown (KD) system (Appendix Fig. S1A,B) combined with in utero electroporation (IUE). We found increased incorporation of EdU by p18 and p27 KD, indicating that more cells entered the S-phase (Fig. 2A,C). Notably, decreased expression of *AldH1l1*-EGFP was observed by p18 and p27 KD, and the effect was enhanced by double KD (Fig. 2B,C). Previous studies reported that p27 KD resulted in defects in the radial migration of postmitotic neurons (Itoh et al, 2007; Nguyen et al, 2006). We confirmed the same effect on neural migration by p27 KD, while no significant change was recognized by p18 KD (Fig. 2D,E). To address the role of CDKIs, we chose p18 as a principal target to investigate because of its specific function in apical progenitors but not neurons. We verified that the reduction in astrocytic differentiation was due to p18 KD because the *AldH1l1*-EGFP signal was rescued by overexpression (OE) of human p18 (Appendix Fig. S1C).

Next, we performed gain-of-function analysis by delivering the p18 gene to apical progenitors. Cell cycle inhibition by p18 OE in target cells was confirmed by reduced incorporation of EdU (Fig. EV2A). OE of p18 in the *AldH1l1*-EGFP mouse brain at E15.5 enhanced the expression of *AldH1l1*-EGFP in subsequent stages toward P0 compared to the control (Fig. 2F,G). Additionally, p18 OE cells localized close to the ventricular surface, while control cells migrated out at P0 (Fig. EV2B). The p18 OE cells near the ventricular surface at P0 showed increased expression of astrocyte markers (Sox9 and GFAP) (Fig. EV2C). These results indicate that

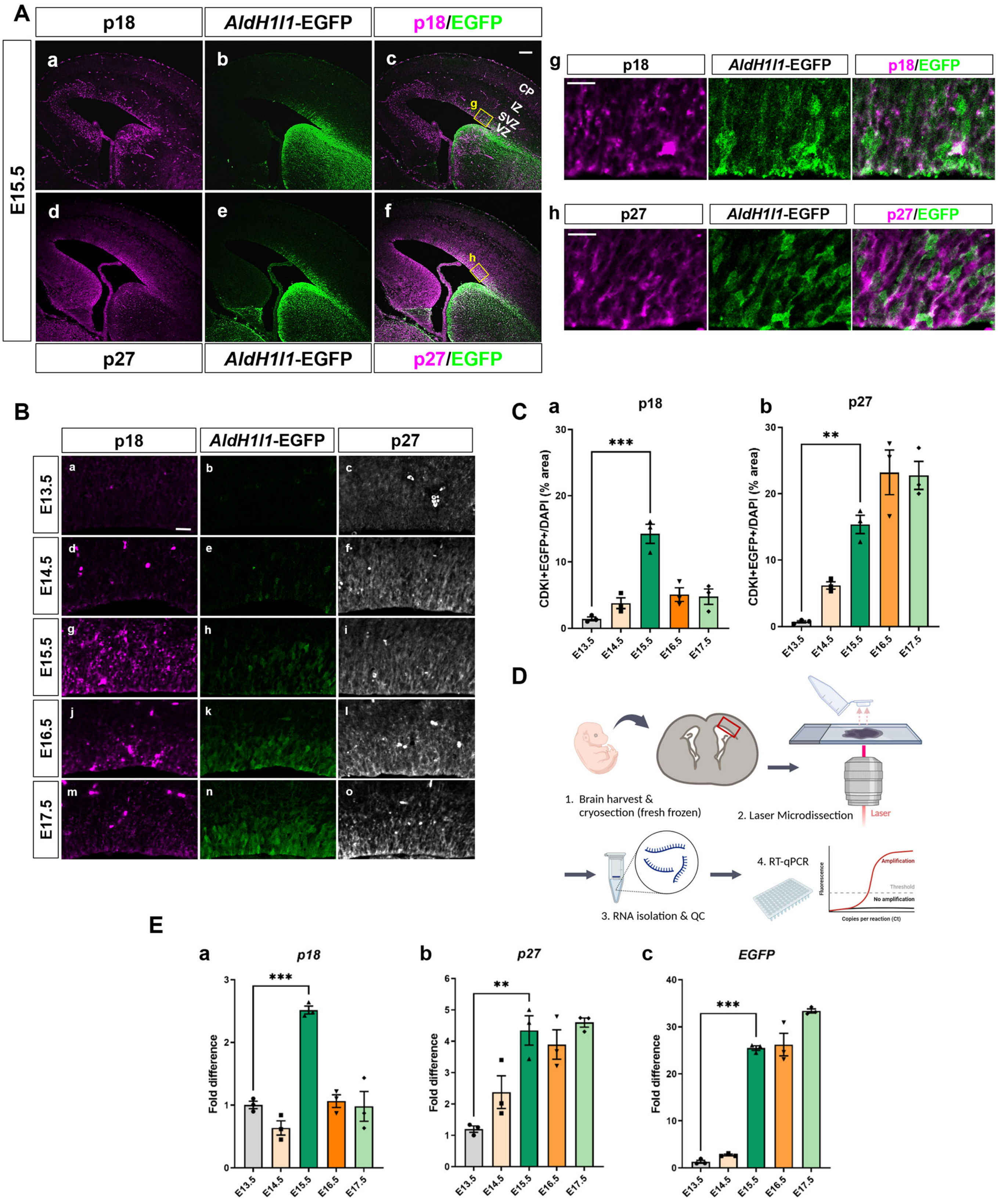
A
p18
AldH1l1-EGFP
p18/EGFP
E15.5
a
b
c
CP
IZ
SVZ
VZ
g
d
e
f
h
p27
AldH1l1-EGFP
p27/EGFP
g
p18
AldH1l1-EGFP
p18/EGFP
h
p27
AldH1l1-EGFP
p27/EGFP
B
p18
AldH1l1-EGFP
p27
E13.5
E14.5
E15.5
E16.5
E17.5
a b c d e f g h i j k l m n o
C
a
p18
***
CDKI+EGFP+/DAPI (% area)
0
10
20
30
E13.5
E14.5
E15.5
E16.5
E17.5
b
p27
**
CDKI+EGFP+/DAPI (% area)
0
10
20
30
E13.5
E14.5
E15.5
E16.5
E17.5
D
1. Brain harvest & cryosection (fresh frozen)
2. Laser Microdissection
Laser
3. RNA isolation & QC
4. RT-qPCR
Fluorescence
Amplification
Threshold
No amplification
Copies per reaction (Ct)
E
a
p18
***
Fold difference
0
1
2
3
E13.5
E14.5
E15.5
E16.5
E17.5
b
p27
**
Fold difference
0
1
2
3
4
5
6
E13.5
E14.5
E15.5
E16.5
E17.5
c
EGFP
***
Fold difference
0
10
20
30
40
E13.5
E14.5
E15.5
E16.5
E17.5

Figure 1. Endogenous expression of p18 and p27 in the embryonic *AldH1l1*-EGFP mouse brain.

(**A**) Low-magnification images of E15.5 brains of *AldH1l1*-EGFP mice stained with p18 (a, c) and p27 (d, f) antibodies. VZ, ventricular zone; SVZ, subventricular zone; IZ, intermediate zone; CP, cortical plate. Bar, 100 µm. High-magnification images of VZ stained with p18 (g) and p27 (h) antibodies. Bar, 20 µm. (**B**) Magnified view of (**A**) near the ventricular surface stained with p18 (a, d, g, j, m) and p27 (c, f, i, l, o) antibodies (E13.5–17.5). Bar, 30 µm. (**C**) Quantification of the CDKIs and EGFP double-positive area in (**B**) ($n = 3$ brains each, normalized by the DAPI-positive area). One-way ANOVA with Tukey's test; error bars show mean ± SEM. ***$P = 0.00003438$ (a), **$P = 0.00200336$ (b). (**D**) Schematics of laser microdissection of brain sections and RNA preparation (created with BioRender.com.). (**E**) qPCR analysis of p18, p27, and *AldH1l1*-EGFP expression in the VZ (E13.5-17.5, $n = 3$ brains). One-way ANOVA with Tukey's test; error bars show mean ± SEM. ***$P = 0.00007995$ (a), **$P = 0.00130536$ (b), ***$P = 0.00000024$ (c). Source data are available online for this figure.

p18 can induce astrocytes, which exhibit distinct migration patterns. Notably, a significant increase in Sox10- and PDGFRalpha-positive cells was not recognized, indicating that p18 OE did not induce the oligodendrocyte lineage (Fig. EV2D). We further tested whether p18 affects astrocyte differentiation in a cell-autonomous manner using an in vitro system of NS cells (Imayoshi et al, 2013). NS cells derived from *AldH1l1*-EGFP Tg mice were maintained in proliferative medium and then switched to astrocytic differentiation conditions after introducing p18-P2A-mKusabiraOrange2 (mKO2) or its control. The presence of p18 caused a significant increase in *AldH1l1*-EGFP expression, suggesting that p18 can induce astrocytic differentiation in a cell-intrinsic manner (Fig. 2H,I).

The function of CDKIs in neural and astrocyte differentiation is stage-dependent

Our results indicate that p18 in apical progenitors at particular developmental stages upregulates *AldH1l1*-EGFP, an astrocyte marker. However, previous reports demonstrated that the introduction of CDKIs or lengthening of the cell cycle enhanced neural production (Calegari and Huttner, 2003; Dehay and Kennedy, 2007; Nguyen et al, 2006). To explore the seemingly conflicting results, we introduced CDKIs to apical progenitors in various stages during cortical development (Fig. 3A,B). When p18 and p27 were electroporated to E12.5, the number of cells positive for Neurogenin2 (Ngn2), a key transcription factor that generates excitatory neurons, increased significantly at E13.5 compared to the control. Notably, Ngn2-positive cells decreased at E15.5 and 16.5 after IUE at E14.5 and 15.5, respectively. This finding suggests that the OE of CDKIs at earlier stages can enhance neural lineage-committed cells while suppressing them at later stages.

There is a possibility that an enhanced signal of *AldH1l1*-EGFP by p18 OE could be a temporal effect and might not mean an increase in terminally differentiated astrocytes. We therefore electroporated p18 in embryonic stages and then dissected brains at P10 when cortical layers are virtually formed (Fig. 3C). We did not find significant changes in the cellular distributions and lineages between p18 OE and the control introduced at E12.5, the period when Ctip2-positive deeper-layer neurons are generated (Fig. 3D; Appendix Fig. S2). The control electroporated cells at E15.5 differentiated into upper-layer (UL) neurons, showing a distribution close to the pial surface due to radial migration. We found ectopic distributions of p18 OE cells at the ventricular surface and internal cortical region in addition to the upper layer. We further investigated the correlation between the position and fate of electroporated cells by using markers of UL neurons (Satb2 and Cux1) and astrocytes (GFAP and S100Beta). Satb2- and Cux1-positive cells in the upper layer were decreased, while GFAP- and S100Beta-positive cells close to the ventricular surface were increased by p18 OE (Fig. 3E). These results suggest that the differentiation lineage was switched from the production of UL neurons to astrocytes by p18 OE introduced at E15.5.

We next examined morphological characteristics at single-cell resolution in the postnatal brain. A limited number of electroporated cells were designed to express membrane-localizing EGFP by Cre-loxP recombination (Fig. 4A). Subsequently, we performed program-based quantifications of the nuclear volume and aspects of the cellular process, including number, length, and directionality (Fig. 4B). When IUE was performed at E14.5 and 15.5 when UL neurons are generated, the nuclear volume was decreased by p18 OE. Importantly, control cells electroporated at E17.5, when astrocytes are primarily produced, showed a smaller nuclear volume (Fig. 4C). Moreover, cellular processes became shorter, and their numbers were increased by p18 OE at E14.5 and 15.5 (Fig. 4D,E). A comparison of process directionality per area divided by angle showed that the polarized shape tended to be lost by p18 OE, which reflects the nonpolar shape of astrocytes (Fig. 4F). Thus, in addition to changes in marker expression, morphological alterations were evoked as a consequence of p18 OE in apical progenitors, which originally ought to produce UL neurons.

Generation of conditional p18-P2A-mKO2 knock-in mice to analyze lineage transition

Our results obtained by IUE indicate that p18 OE induces switching from neural to astrocytic differentiation in a developing stage-dependent manner. To analyze the molecular basis of the lineage transition in a more robust system than IUE, we generated a conditional knock-in mouse containing a loxP-flanked stop sequence and p18-P2A-mKO2 in the ROSA26 locus (Fig. 5A). We first delivered the Cre gene by IUE to confirm the production of p18 and mKO2 (Appendix Fig. S3A). We crossed the p18-P2A-mKO2 mouse to the Nestin-CreER^{T2} line (Imayoshi et al, 2006) to allow the expression of p18-P2A-mKO2 in apical progenitors upon tamoxifen administration. The mKO2 signal was observed after Cre-loxP recombination in the brains of NesCreER^{T2}/p18-P2A-mKO2 double-positive mice but not in controls (Appendix Fig. S3B–F). To examine the effect of p18 in NSCs by histological analysis, we injected EdU into pregnant mice to label the proliferating cell population prior to tamoxifen administration at E15.5. The EdU incorporation patterns were essentially the same between the double-positive and control littermates. We found an increase in AldH1l1-positive cells and a decrease in Ngn2-positive cells among EdU-positive cells at E16.5 (Fig. 5B,C). Moreover, Satb2-positive cells in the UL were decreased, while AldH1l1- and Sox9-positive cells close to the ventricular surface increased in the P10 brains (Fig. 5D,E), validating that the lineage transition from

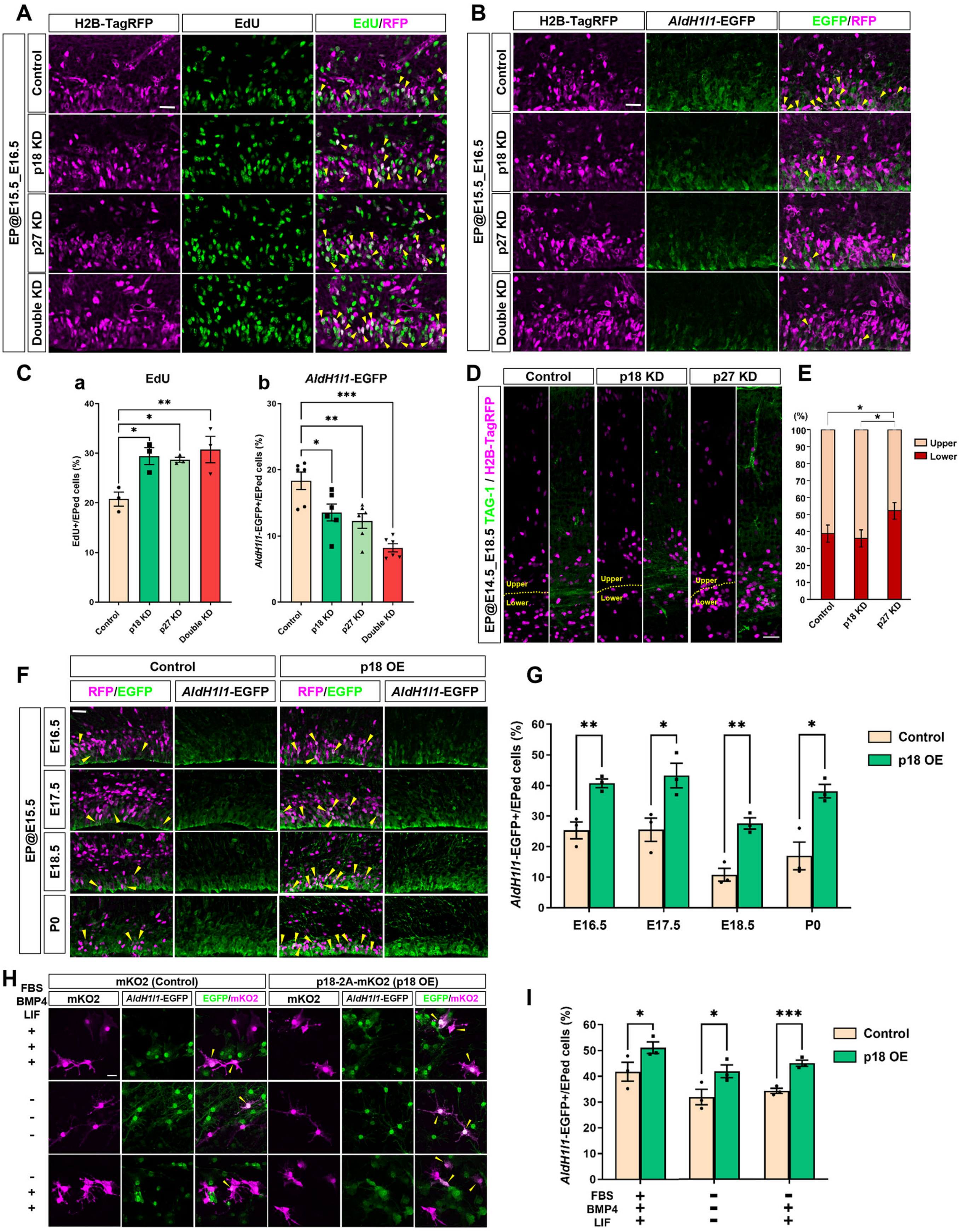
A
H2B-TagRFP
EdU
EdU/RFP
EP@E15.5_E16.5
Control
p18 KD
p27 KD
Double KD
B
H2B-TagRFP
AldH1l1-EGFP
EGFP/RFP
EP@E15.5_E16.5
Control
p18 KD
p27 KD
Double KD
C
a
EdU
EdU+/EPed cells (%)
0
10
20
30
40
*
*
**
Control
p18 KD
p27 KD
Double KD
b
AldH1l1-EGFP
AldH1l1-EGFP+/EPed cells (%)
0
10
20
30
*
**
***
Control
p18 KD
p27 KD
Double KD
D
Control
p18 KD
p27 KD
EP@E14.5_E18.5 TAG-1 / H2B-TagRFP
Upper
Lower
E
(%)
0
10
20
30
40
50
60
70
80
90
100
*
*
Upper
Lower
Control
p18 KD
p27 KD
F
Control
p18 OE
RFP/EGFP
AldH1l1-EGFP
RFP/EGFP
AldH1l1-EGFP
EP@E15.5
E16.5
E17.5
E18.5
P0
G
AldH1l1-EGFP+/EPed cells (%)
0
10
20
30
40
50
60
**
*
**
*
E16.5
E17.5
E18.5
P0
Control
p18 OE
H
FBS
BMP4
LIF
mKO2 (Control)
p18-2A-mKO2 (p18 OE)
mKO2
AldH1l1-EGFP
EGFP/mKO2
mKO2
AldH1l1-EGFP
EGFP/mKO2
+
+
+
-
-
-
-
+
+
I
AldH1l1-EGFP+/EPed cells (%)
0
10
20
30
40
50
60
*
*
***
Control
p18 OE
FBS
BMP4
LIF
+
+
+
-
-
-
-
+
+

Figure 2. Functional analysis of p18 and p27 in the developing dorsal cortex.

(**A**) Plasmids to induce KD of p18 and p27 mixed with pCAG-H2B-TagRFP were delivered at E15.5 to *AldH1l1*-EGFP mice. EdU was administered 2 h before fixation at E16.5. Arrowheads; double-positive cells to EdU and H2B-TagRFP. Bar, 50 µm. (**B**) The expression of *AldH1l1*-EGFP prepared in (**A**). Arrowheads; double-positive cells to *AldH1l1*-EGFP and H2B-TagRFP. Bar, 50 µm. (**C**) Quantification of the stained images shown in (**A**) ($n = 3$ brains each) and (**B**) ($n = 6$ sections from 3 brains each). Total counted cells of Control, p18 KD, p27 KD, Double KD; *331, 433, 363, 420*. One-way ANOVA with Tukey's test; error bars show mean ± SEM. From left to right, *$P = 0.02035068$, *$P = 0.03126960$, **$P = 0.00955672$ (a), *$P = 0.01734001$, **$P = 0.00268600$, ***$P = 0.00000817$ (b). (**D**) Plasmids to induce KD of p18 and p27 mixed with pCAG-H2B-TagRFP were delivered at E14.5 and then fixed at E18.5. Sections were stained using TAG-1 antibody to recognize axon fibers as the border between the upper and lower positions. Bar, 50 µm. (**E**) Quantification of the stained images shown in (**D**) ($n = 4$ brains each). Total counted cells of Control, p18 KD, p27 KD; *544, 614, 429*. One-way ANOVA with Tukey's test; error bars show mean ± SEM. From left to right, *$P = 0.04727532$, *$P = 0.01171081$. (**F**) Plasmids to induce OE of p18 mixed with pCAG-H2B-TagRFP were delivered at E15.5 to *AldH1l1*-EGFP mice and then fixed at E16.5-P0. Arrowheads; double-positive cells to *AldH1l1*-EGFP and H2B-TagRFP. Bar, 50 µm. (**G**) Quantification of the stained images shown in (**F**) ($n = 3$ brains each). Total counted cells of Control, p18 OE*; 256, 274* (E16.5)*; 400, 449* (E17.5)*; 390, 473* (E18.5)*; 253, 365* (P0). Two-tailed *t* test; error bars show mean ± SEM. From left to right, **$P = 0.00752188$, *$P = 0.03272830$, **$P = 0.00392106$, *$P = 0.01368411$. (**H**) pCAG-mKO2 or pCAG-p18-P2A-mKO2 were transfected into cultured NS cells prepared from *AldH1l1*-EGFP mouse brains, followed by induction to astrocytes using the conditions indicated on the left. Arrowheads; double-positive cells to *AldH1l1*-EGFP and H2B-TagRFP. Bar, 20 µm. (**I**) Quantification of the stained images shown in (**H**) ($n = 3$, independent culture each). Total counted cells of Control, p18 OE*; 220, 296* (FBS + BMP4 + LIF +)*; 140, 170* (FBS- BMP4-LIF-)*; 195, 380* (FBS-BMP4 + LIF +). Two-tailed *t* test; error bars show mean ± SEM. From left to right, *$P = 0.04486357$, *$P = 0.02332944$, *$P = 0.00392106$, ***$P = 0.00050115$. Source data are available online for this figure.

UL neurons to astrocytes occurred in the p18 knock-in mouse brain, equivalent to the results of IUE.

Global gene expression profiling in neural and glial differentiation by p18 in NSCs

To reveal the molecular and genetic network involved in neural and glial differentiation invoked by p18 OE, we designed a transcriptome analysis to compare differential gene expression in NSCs at earlier and later embryonic stages. We applied tamoxifen at E12.5 and 15.5 and then prepared RNA from NesCreER^{T2}/p18-P2A-mKO2 littermates (hereafter mKO2- or mKO2 +) from the VZ in the dorsal cortex cut by LMD at E13.5 and 16.5, respectively (datasets were named *E13* and *E16*). The short induction period after tamoxifen administration enables the acquisition of gene sets expressed by the immediate response and minimizes the possibility of the inclusion of cells produced outside of the dorsal cortical VZ. A total of 2,828 and 354 genes were differentially expressed between *E16* and *E13* for mKO2- (equivalent to normal development) and mKO2 + , respectively (Fig. 6A,B), although comparisons between mKO2- and mKO2+ at each stage showed fewer differences (Fig. EV3A). As landmark molecules, we observed elevated expressions of neural markers (*Map2* and *Nptx1*) and astrocyte markers (*Aldh1l1* and *Gfap*) in *E13* and *E16*, respectively, in mKO2+ (Fig. EV3B). The expression of *p27* (*Cdkn1b*) showed no difference between mKO2- and mKO2+ (Fig. EV3C). Functional enrichment analysis (Fig. 6C,D) revealed that differentially expressed genes (DEGs) at *E16* relative to *E13* in mKO2- embryos (hereafter mKO2-$^{E16/E13}$) were enriched in biological pathway terms associated with the cell cycle (top 1st, 7th, and 11th) but not in mKO2 +$^{E16/E13}$, reflecting that the proliferation of NSCs in mKO2+ embryos was arrested. Importantly, notable pathways like "*Glial cell development*" (GO:0021782) and "*Delta-Notch signaling pathway*" (WP265) were identified in mKO2 +$^{E16/E13}$. Other pathways were largely overlapped in both mKO2-$^{E16/E13}$ and mKO2 +$^{E16/E13}$. In mKO2 +$^{E16/E13}$, DEGs involved in *Glial cell development*, such as *Adora2a* and *GFAP*, were upregulated, while *Dll1* and *Hes5*, related to the maintenance of stem cell features in the Notch signaling pathway, were downregulated, implying that differentiation to the glial lineage was promoted in mKO2 +$^{E16/E13}$.

To further compare the cell type composition, deconvolution of gene expression (BayesPrism) was performed combined with published mouse forebrain scRNA-seq data (La Manno et al, 2021) (Fig. EV3D). As a reference, clusters from the scRNA-seq data were annotated to distinct subtypes of Neuron (excitatory), Intermediate progenitor (Basal progenitor, positive for *Eomes/Tbr2*), Radial glia, and GABAergic (interneuron) by their marker genes (Fig. EV3E,F). A significant increase in the proportion of Neuron and a steep decrease in the proportion of Radial glia in mKO2+ compared to mKO2- were observed in *E13*, while there was no change in the proportion of Intermediate progenitor (Fig. 6E). This suggests that p18 promotes differentiation to the lineage of excitatory neurons at E13.5 by consuming apical progenitors. Notably, the proportion of Astrocyte was significantly increased in both *E13* and *E16*, while the proportions of Neuron, Radial glia, Intermediate progenitor, and Oligodendrocyte were neither increased nor decreased in *E16*. The proportion of GABAergic was also slightly increased in both *E13* and *E16*, although there was no statistical significance.

The top 50 differentially expressed genes were investigated to screen whether there were any functional differences in each cell type (Figs. 6F and EV3G). In Neuron, genes related to neural development, such as *Mef2c* and *Rbfox1*, were upregulated in mKO2+ only in *E13*, which might explain the experimental results that p18 OE induces the neural lineage at E13.5 but not at E16.5. In Astrocyte, upregulated expression of genes related to astrocyte development (*AldH1l1* and *Tnc*) was recognized in *E13*. Taken together with the results in Fig. 6E, it can be speculated that p18 OE may initiate astrocyte differentiation at E13.5. Of note, the proportion of increased Astrocyte was minor compared to the increased proportion of Neuron in *E13*, while only Astrocyte was increased in *E16* (Fig. 6E). Interestingly, Dlx-family genes, as well as marker genes of interneurons (*Gad1*, *Gad2*), were highly expressed in GABAergic in mKO2+ (Fig. 6F). These results demonstrate that p18 OE has a wide range of effects on the transcriptome related to the lineage transition of neurons and glial cells.

Using NesCreER^{T2}/p18-P2A-mKO2 mice, we also investigated whether the methylation status of genomic DNA changes by p18 OE. Although we found a decrease in CpG methylation at the promoter region of *GFAP* along the developmental stage as previously reported (Takizawa et al, 2001), we could not find significant differences between mKO2- and mKO2+ both at E13.5 and E16.5 (Fig. EV4).

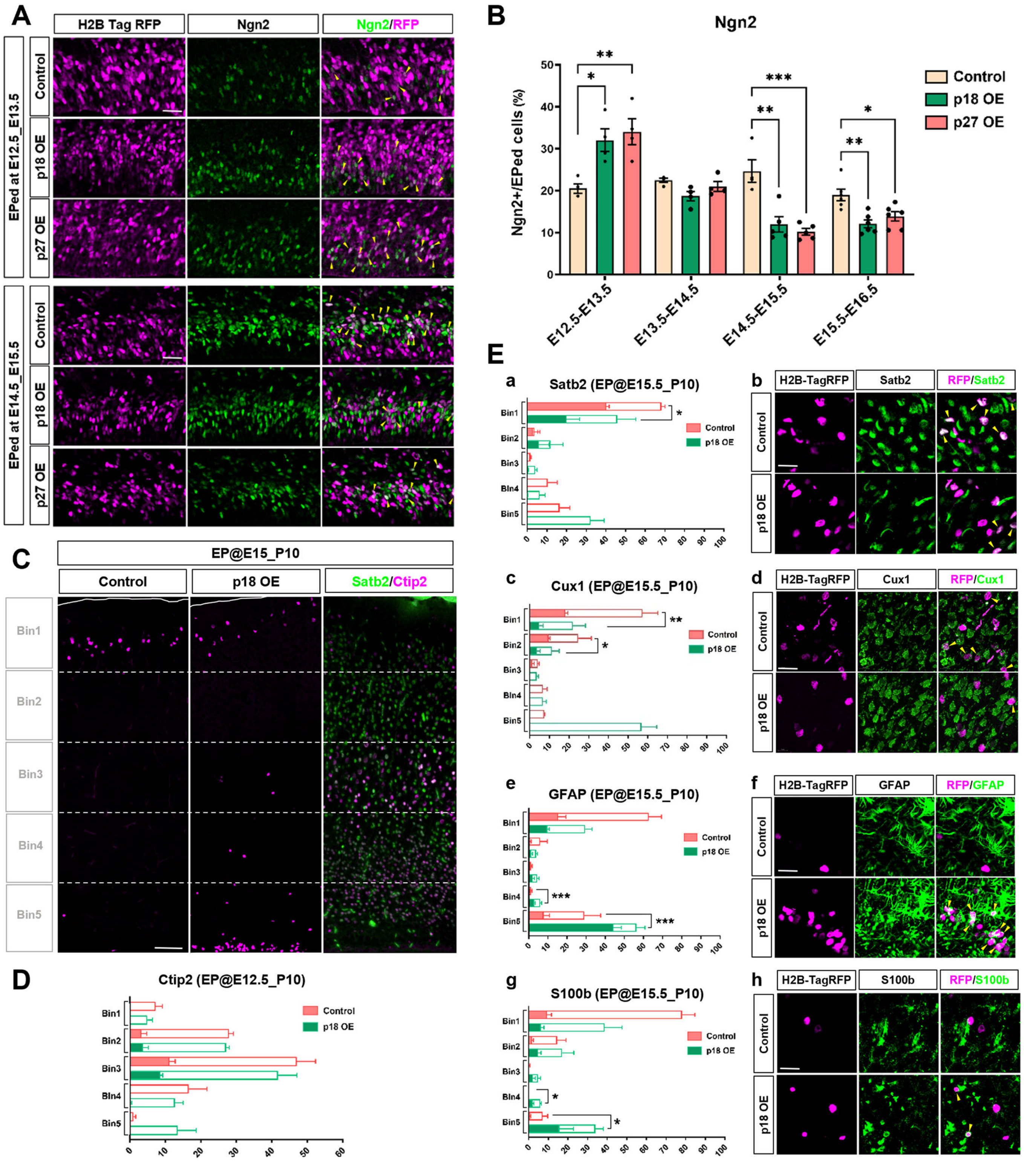

Expression and function of Dlx2 in the dorsal cortical lineage

Our transcriptome analysis revealed that Dlx-family genes (*Dlx1, 2, 5,* and *6*) were upregulated at E16.5 in NesCreER^{T2}/p18-P2A-mKO2 mice (Fig. 6F). We validated the upregulation of *Dlx2* in p18-electroporated dorsal cortical cells by qPCR (Appendix Fig. S4A). Dlx-family genes have been well studied as neurogenic genes in the GE-originated cells (Achim et al, 2014). However, lineage analyses using transgenic reporter mice (Kohwi et al, 2007) and scRNAseq (Li et al, 2021) have shown that Dlx-family genes are also expressed in a certain number of cells in the dorsal cortical lineage. Notably,

Figure 3. Stage-dependent functions of CDKIs.

(**A**) Plasmids to induce OE of p18 and p27 mixed with pCAG-H2B-TagRFP were delivered at E12.5, 13.5, 14.5, and 15.5 and then fixed after 1 d. Sections were stained using Ngn2 antibody. Images after IUE at E12.5 and 14.5 are presented. Arrowheads; double-positive cells to Ngn2 and H2B-TagRFP. Bar, 50 µm. (**B**) Quantification of Ngn2-positive cells among H2B-TagRFP-positive cells ($n = 4$–6 brains). Total counted cells of Control, p18 OE, p27 OE; *262, 257, 155* (E12.5EP); *262, 199, 269* (E13.5EP); *229, 274, 225* (E14.5EP); *443, 375, 450* (E15.5EP). One-way ANOVA with Tukey's test; error bars show mean ± SEM. From left to right, $^{*}P = 0.02269181$, $^{**}P = 0.00939859$, $^{**}P = 0.00130391$, $^{***}P = 0.00046411$, $^{**}P = 0.00199138$, $^{*}P = 0.01730243$. (**C**) Plasmids to induce OE of p18 with pCAG-H2B-TagRFP were delivered at E15.5 and then fixed at P10. Bar, 100 µm. (**D**) Quantification of Ctip2-positive cells among H2B-TagRFP-positive cells. Plasmids to induce OE of p18 with pCAG-H2B-TagRFP were delivered at E12.5 and then fixed at P10 ($n = 3$ brains). Total counted cells of Control, p18 OE; *975, 1282*. Two-tailed *t* test; error bars show mean ± SEM. No statistically significant differences were detected. (**E**) (a, c, e, g) Quantification of Satb2 (a), Cux1 (c), GFAP (e), and S100beta (g)-positive cells among H2B-TagRFP-positive cells ($n = 3$–7 brains). Total counted cells of Control, p18 OE; *381, 639* (Satb2); *195, 194* (Cux1); *281, 560* (GFAP); *409, 488* (S100beta). Two-tailed *t* test; error bars show mean ± SEM. From top to bottom, $^{*}P = 0.04268962$ (a), $^{**}P = 0.00460726$, $^{*}P = 0.02607529$ (c), $^{***}P = 0.00056828$, $^{***}P = 0.00001354$ (e), $^{*}P = 0.01101942$, $^{*}P = 0.01365471$ (g). (b, d, f, h) Magnified images of sections stained by Satb2 (b; BIN1), Cux1 (d; BIN1), GFAP (f; BIN5), and S100beta (h; BIN5). Bar, 20 µm. Arrowheads; double-positive cells to H2B-TagRFP and Satb2 (b), Cux1 (d), GFAP (f), or S100b (h). (**C–E**) the entire span of the cortex was divided equally into 5 portions (BIN). BIN 1: pial side/BIN 5: ventricular side (same for Figs. 5D,E and 8C). The open (outside) bars indicate the ratio of H2B-TagRFP-positive cells in each BIN among all BINs, whereas the solid (inside) bars indicate positive cells (Ctip2 for **D**; Satb2, Cux1, GFAP, and S100beta for **E**) among RFP-positive cells. *t* tests were performed for solid bars in the same BIN. Source data are available online for this figure.

the latter analysis reported that Dlx-family genes are expressed in multipotent intermediate progenitor cells (MIPCs), which can produce OB interneurons.

Here, we addressed the expression pattern of endogenous Dlx2 using Emx1-Cre/Ai9 mice, which labels dorsal cortex-originated cells with tdTomato (Fig. 7A). Interestingly, in the VZ and the subventricular zone (SVZ) at E17.5, 35% or 41% of Dlx2- or Ngn2-positive cells, respectively, were tdTomato positive, but only a few cells (<6%) were triple positive for Ngn2, Dlx2, and tdTomato (Fig. 7A). We then performed IUE targeting the dorsal VZ at E15.5. Brains dissected at E16.5-18.5 showed that, in controls, 5-7% of EGFP-positive cells were Dlx2-positive cells; those were increased to 14% at the perinatal stage in the case of p18 OE (Fig. 7B,C). We next conducted functional tests of Dlx2 in dorsal cortex-derived cells using Dlx2 OE and KD (Appendix Fig. S4B) constructs. We found that the number of Ngn2-positive cells was decreased by Dlx2 OE while increased by Dlx2 KD (Fig. 7D,E). We further explored whether Dlx2 can directly affect the promoter of *Ngn2* by luciferase assay. Indeed, Dlx2 suppressed the promoter activity of *Ngn2* as Hes1, a well-characterized suppressor of *Ngn2* (Shimojo et al, 2008), did (Fig. 7F). Notably, the number of AldH1l1-positive cells was decreased by Dlx2 OE while increased by Dlx2 KD (Fig. 7G,H).

Sequential regulation of lineages by p18: UL neurons, astrocytes, and OB interneurons

Functional analysis of Dlx2 raised the possibility that augmented Dlx2 by p18 might subsequently induce OB interneurons by suppressing astrocytes in the later stage. To characterize the mutual relations of each lineage, we performed OE of p18 and Dlx2 at E15.5 followed by immunostaining of E18.5 brains using markers of UL neurons (Satb2), astrocytes (AldH1l1 and Sox9), and OB interneurons (Sp8) (Fig. 8A,B). Both p18 and Dlx2 OE suppressed UL neurons; astrocytes were increased by p18 and decreased by Dlx2. OB interneurons were strongly increased by Dlx2. Interestingly, more cells were located in the basal region of the cortex in the control group and close to the ventricular surface in the p18 OE group and in the SVZ in the Dlx2 OE group (Fig. 8A), indicating that the induction of different lineages altered cellular localization. We further addressed the effects of p18 and Dlx2 OE in the postnatal stages. Upregulation of Dlx2 by p18 OE was prominent near the ventricular surface at P1 (Fig. 8C). Importantly, p18 and Dlx2 OE cells were identified in the rostral migratory stream (RMS) with Sp8 expression at P4, displaying their ability to migrate toward the OB (Fig. 8D).

The results of immunostaining and qPCR revealed that p18/p27 double KD increased UL neurons and reduced OB interneurons (Fig. 8E,F; Appendix Fig. S5). We next investigated the effect of Dlx2 KD on lineage determination. In contrast to Dlx2 OE, Dlx2 single KD increased UL neurons and astrocytes compared to the control at E18.5 (Fig. 8G,H). Since p18 enhanced the expression of Dlx2, we addressed the possibility of whether the removal of Dlx2 can strengthen the effect of p18 OE to elevate astrocyte induction. We performed combined IUE of p18 OE and Dlx2 KD, which resulted in more astrocytes than p18 single OE (Fig. 8G,H).

Finally, to further clarify whether the lineage transitions occur at the single cell level or distinct subsets in each lineage, we utilized piggyBac (PB)-*Gfa2*-EGFP, the transposon-based fluorescent reporter of the astrocyte lineage (Hamabe-Horiike et al, 2021). Chromosome-integrated PB-RFP introduced by IUE allows labeling all clones derived from electroporated NSCs. Once astrocyte lineage is induced, the cell becomes EGFP-positive, then the EGFP signal remains as the footprint. We verified that the *Gfa2*-EGFP was upregulated by p18 OE while downregulated by p18/p27 double KD, similar to AldH1l1 and Sox9 (Fig. 9A–C). Remarkably, Dlx2/RFP double-positive cells with *Gfa2*-EGFP signal were prominently increased by p18 OE at the perinatal stage (E17.5 and P1) (Fig. 9D,E). Moreover, Sp8-positive cells in the RMS were increased by p18 OE (28% among RFP-positive cells) compared to the control (14%) at P4. With p18 OE, 67% of Sp8/RFP double-positive cells exhibited the EGFP signal (Fig. 9D,E). These results confirm the view that p18 facilitates lineage transitions from NSC to OB interneuron via astrocyte within a single cell's progeny.

Discussion

CDKIs, cell cycle, and differentiation

The conceptual novelty of this study can be summarized as follows: (1) the role of CDKIs differs between early and late stages of brain development; (2) p18 facilitates lineage transitions of excitatory neurons, astrocytes, and interneurons. Regarding the first point, we

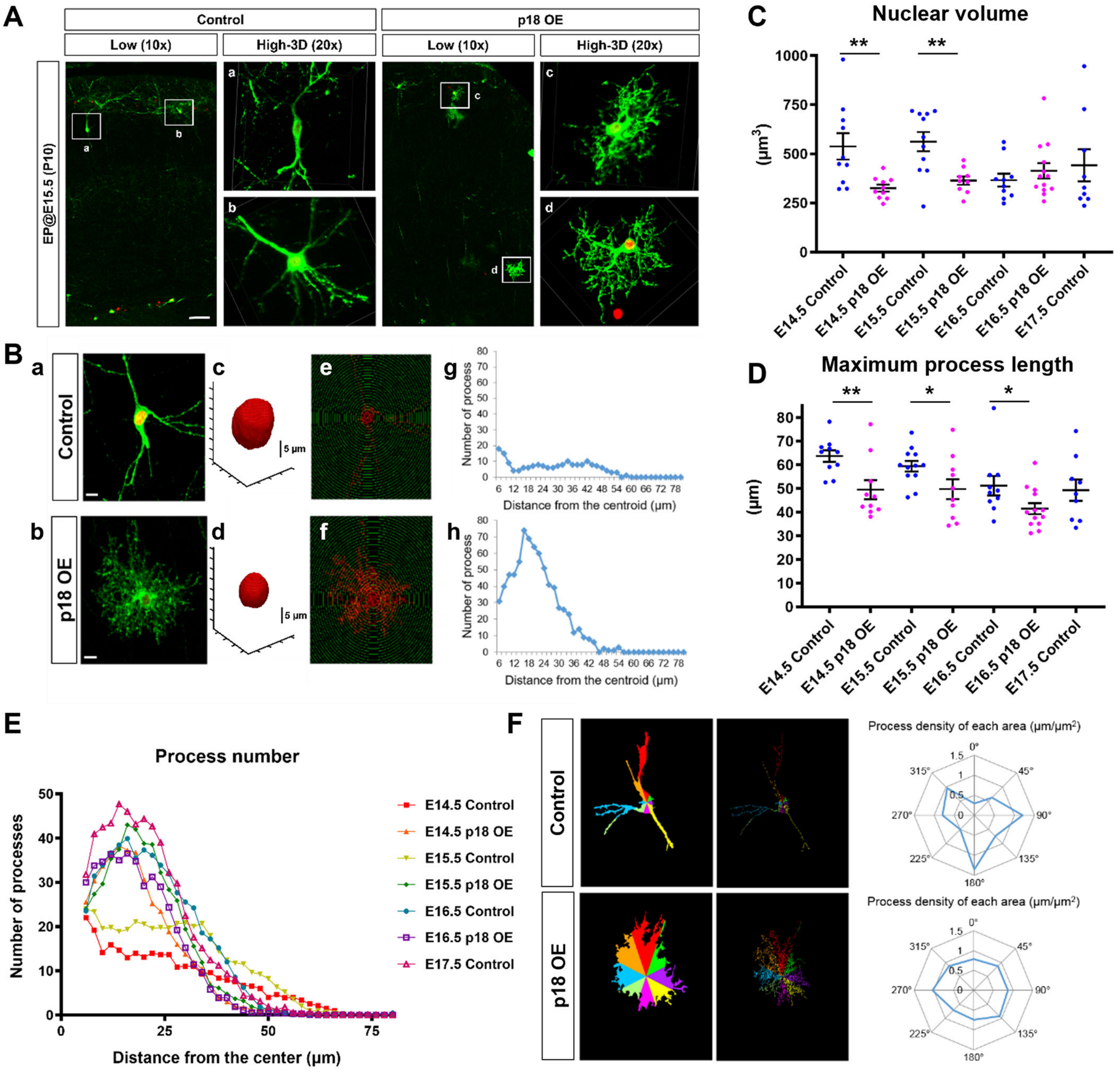

Figure 4. Quantitative morphological analysis of p18 OE cells at single-cell resolution.

(**A**) For the labeling of individual cell shapes, plasmids to induce OE of p18 with pCAG-H2B-TagRFP, pCAG-FloxP-EGFP-F, and pCAG-Cre were delivered at E14.5-17.5 and then fixed at P10. Low magnification and 3D-reconstructed images are exhibited. Bar, 50 μm. (**B**) Examples of the morphological analysis. Cells without overlapping were chosen (a and b), and then the nuclear shape was deconvoluted (c and d). After the calculation of the centroid, a Sholl analysis using the 2D-projected image was performed (e and f) and then analyzed (g and h). Bar, 10 μm. (**C**) Comparison of nuclear volume at P10 after IUE at E14.5, 15.5, and 16.5 for the control and p18 ($n = 10, 10, 11, 9, 10, 13, 9$, from the left of the graph). For the control, the IUE at E17.5, the stage of dominant production of endogenous astrocytes, was also tested. Two-tailed *t* test; error bars show mean ± SEM. From left to right, $^{**}P = 0.00666581$, $^{**}P = 0.00293175$. (**D**) Comparison of maximum process length among the conditions indicated in (**C**) ($n = 10, 10, 12, 10, 10, 13, 9$, from the left of the graph). Two-tailed *t* test; error bars show mean ± SEM. From left to right, $^{**}P = 0.00738915$, $^{*}P = 0.04504341$, $^{*}P = 0.04259063$. (**E**) Results of the Sholl analysis. Averaged numbers of 9 samples for each condition are presented. (**F**) Examples showing the relation between the angle and density of processes (scored by the total length of processes per colored area) at P10 after the IUE at E15.5. Source data are available online for this figure.

found that p18 induced neurons in the earlier stage of cortical development and astrocytes in the later stage with reduced UL neurons, while loss of p18/p27 function had the opposite effect. Regarding the second point, surprisingly, p18 evoked the expression of Dlx-family genes, which subsequently induced OB interneuron and suppressed excitatory neurons and astrocytes at the perinatal stage. Thus, our study describes the integrated function of p18 to determine the lineage boundaries (excitatory

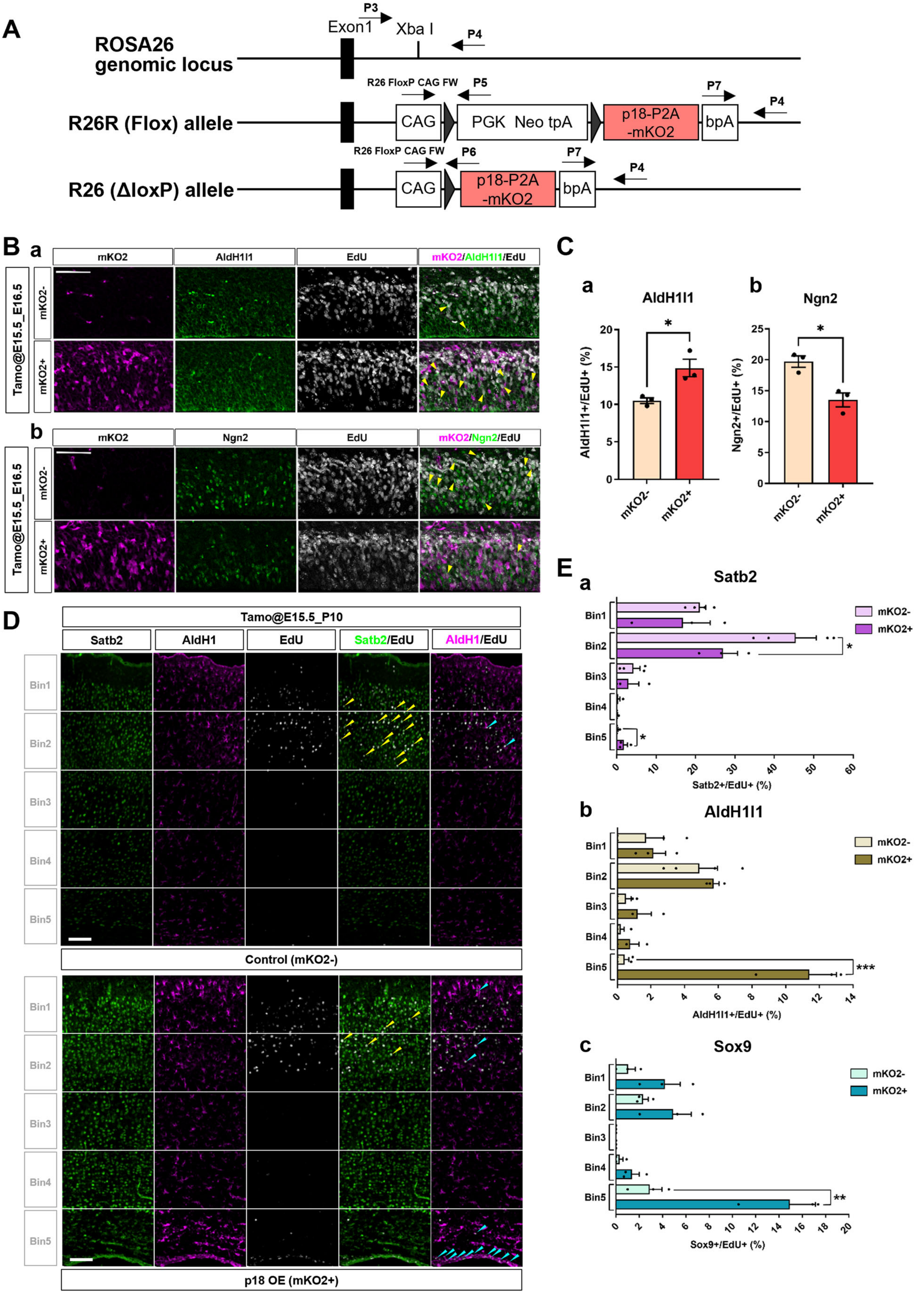
A
ROSA26 genomic locus
Exon1
P3
Xba I
P4
R26R (Flox) allele
R26 FloxP CAG FW
P5
CAG
PGK Neo tpA
p18-P2A -mKO2
P7
bpA
P4
R26 (ΔloxP) allele
R26 FloxP CAG FW
P6
CAG
p18-P2A -mKO2
P7
bpA
P4
B a
mKO2
AldH1l1
EdU
mKO2/AldH1l1/EdU
Tamo@E15.5_E16.5
mKO2-
mKO2+
b
mKO2
Ngn2
EdU
mKO2/Ngn2/EdU
Tamo@E15.5_E16.5
mKO2-
mKO2+
C
a
AldH1l1
AldH1l1+/EdU+ (%)
*
mKO2-
mKO2+
b
Ngn2
Ngn2+/EdU+ (%)
*
mKO2-
mKO2+
D
Tamo@E15.5_P10
Satb2
AldH1
EdU
Satb2/EdU
AldH1/EdU
Bin1
Bin2
Bin3
Bin4
Bin5
Control (mKO2-)
p18 OE (mKO2+)
E
a
Satb2
mKO2-
mKO2+
Satb2+/EdU+ (%)
b
AldH1l1
AldH1l1+/EdU+ (%)
***
c
Sox9
Sox9+/EdU+ (%)
**

Figure 5. Generation and characterization of R26R-p18-P2A-mKO2 Tg mice.

(**A**) Constructs for Tg mouse generation. Arrows indicate primers for genotyping. (**B**) To label proliferating neural progenitors, EdU was injected into pregnant R26R-p18-P2A-mKO2/Nes-CreER^{T2} mice 4 h prior to tamoxifen administration at E15.5, followed by fixation at E16.5. Sections were stained using AldH1l1 (a) and Ngn2 (b) antibodies with EdU detection. Arrowheads; double-positive cells to EdU and AldH1l1 (a) or Ngn2 (b). Bar, 100 µm. (**C**) Quantification of the stained images shown in (**B**) ($n = 3$ brains each). Total counted cells of mKO2-, mKO2 +; *571, 523* (AldH1l1); *488, 444* (Ngn2). Two-tailed *t* test; error bars show mean ± SEM. *$P = 0.02391804$ (a), *$P = 0.01248425$ (b). (**D**) Mice were prepared as indicated in (**B**), and then pups were fixed at P10. Sections were stained using Satb2, AldH1l1, and Sox9 antibodies with EdU detection. Arrowheads; double-positive cells to EdU and Satb2 (yellow) or AldH1l1 (light blue). Bar, 100 µm. (**E**) Quantification of images in (**D**). The bars indicate the proportions of Satb2 (a)-, AldH1l1 (b)-, and Sox9 (c)-positive cells among EdU-positive cells in each BIN. *t* tests were performed between the control and p18 in the same BINs ($n = 3$–4 brains each). Total counted cells of mKO2-, mKO2 +; *385, 486* (Satb2 + /EdU + , AldH1l1 + /EdU +); *305, 345* (Sox9 + /EdU +). Two-tailed *t* test; error bars show mean ± SEM. From top to bottom, *$P = 0.04270011$, *$P = 0.04262900$ (a), ***$P = 0.00024186$ (b), **$P = 0.00392151$ (c). Source data are available online for this figure.

neurons/glial cells/OB interneurons) that emerge sequentially in the dorsal cortex (Fig. 9F, model), which could fill one of the missing links in the lineage specification of multipotent NSCs. Of note, not all p18-activated cells eventually turn into OB interneurons by functions of Dlx-family genes. We consider that the following factors are likely to affect lineage determination between astrocytes and OB interneurons: (1) genetic and epigenetic elements of astrocyte differentiation (see Introduction) and (2) the timing of OB interneuron induction via Dlx-family genes.

Previous studies of CDKIs in regard to neural fate mostly investigated the Cip/Kip family rather than the Ink4 family. Here, we explored the functions of p18 (Ink4) and p27 (Cip/Kip), which show increased expression in NSCs at the onset of glial production. Both the Ink4 and Cip/Kip families regulate CyclinD-Cdk4/6, while Cip/Kip also inactivates CyclinE-Cdk2, CyclinA-Cdk2, and CyclinB-Cdk1 (Grison and Atanasoski, 2020; Schirripa et al, 2022). Then, what are the roles of components other than CDKIs in NSCs? Double Cdk4/Cdk6 KO mice showed a reduction in intermediate progenitors, while Cdk2/Cdk6 had little effect on progenitor proliferation (Grison et al, 2018). Double KD of Cdk4 and CyclinD1 caused a prolonged cell cycle of apical progenitors and increased neurogenesis (Lange et al, 2009). More recently, it was reported that CyclinB1/2 and CyclinD1 have significant roles in controlling the differentiation of cortical progenitors (Hagey et al, 2020). The expression of Slc1A3/Glast, a marker of RGCs and astrocytes (Mori et al, 2006), was downregulated by CyclinD1 gain-of-function while upregulated by its loss-of-function. This result is consistent with our findings that the acquisition of glial cell features is regulated by cell cycle controllers. CyclinB1/2 had opposite effects, which is explained by the altered cell division mode (symmetric vs. asymmetric) of NSCs and Notch signaling (Hagey et al, 2020). Our in vitro study (Fig. 2) supports the view that the p18-dependent regulation of differentiation can be autonomous. However, the combined effects of autonomous and non-autonomous might be involved in vivo. Indeed, our RNAseq analysis of microdissected tissue implies the involvement of the Delta-Notch pathway in p18 OE conditions (Fig. 6). Further comprehensive analyses would uncover the mutual relationships of CDKIs, cyclins, and other cell cycle regulators to control lineage transitions of cortical NSCs.

Multilineage potency of NSCs in the dorsal cortex

Traditionally, it has been well described that excitatory neurons are produced in the dorsal cortex, while GABAergic interneurons are generated in the GE (Achim et al, 2014). In particular, OB interneurons are generated at the LGE and reach the OB via the RMS (Waclaw et al, 2006). As mentioned in the Results, a more recent lineage study using scRNAseq revealed the existence of MIPCs in the dorsal cortical wall at the perinatal stage (Li et al, 2021; Zheng et al, 2022). At approximately E16.5, RGCs start to transform into apical MIPCs (aMIPCs). Subsequently, aMIPCs rapidly become bMIPCs, which can give rise to astrocytes, oligodendrocytes, and OB interneurons. Notably, the scRNA-seq results indicate that the expression of Mki67 and Cdk1, markers of cell proliferation, is rarely detectable in aMIPCs (Li et al, 2021). Given that p18 inhibits cell cycle progression, a reduction in proliferation might be required to transform RGCs into aMIPCs. Another interesting point is that bMIPCs gradually show the features of OB intermediate progenitor cells by expressing Dlx-family genes and then eventually differentiate into Sp8/9-positive OB interneurons (Li et al, 2021). Here, our results showed that Dlx2 OE suppressed the lineage of astrocytes, while loss of Dlx2 function induced more astrocyte populations. These findings suggest that the expression of Dlx-family genes in bMIPCs can determine the lineage between astrocytes and OB interneurons. It has also been reported that forced expression of Dlx2 at the earlier developmental stage induces local accumulation of cells showing OB interneuron markers (Guo et al, 2019). Importantly, our results demonstrate that OB interneurons produced by Dlx2 OE reach the OB through chain migration at the neonatal stage (Fig. 8). Taken together, it can be deduced that the expression of Dlx-family genes should be at the proper timing to produce interneurons with migration ability to reach the OB.

Influences of lineage choice on brain size and architecture

Our results demonstrate that the expression level of p18 determines the boundary among lineages that appear from NSCs in the developing mammalian cortex. As a result, the ratio and localization of each cell type born at the given time differed in the late embryonic and postnatal stages. Based on the findings, we deduce a unique possibility that the timing of CDKI expression in the developing stage can be one of the vital factors that influence diverse brain sizes and architecture among species. Indeed, a previous study using KO mice described the increased size of general organs in p18 and p27 null mice, although a detailed histological analysis of the brain architecture is still required (Franklin et al, 1998). Investigations of spatiotemporal expression patterns of CDKIs in the developing brains of several species and manipulations of their functions in vivo using model animals or

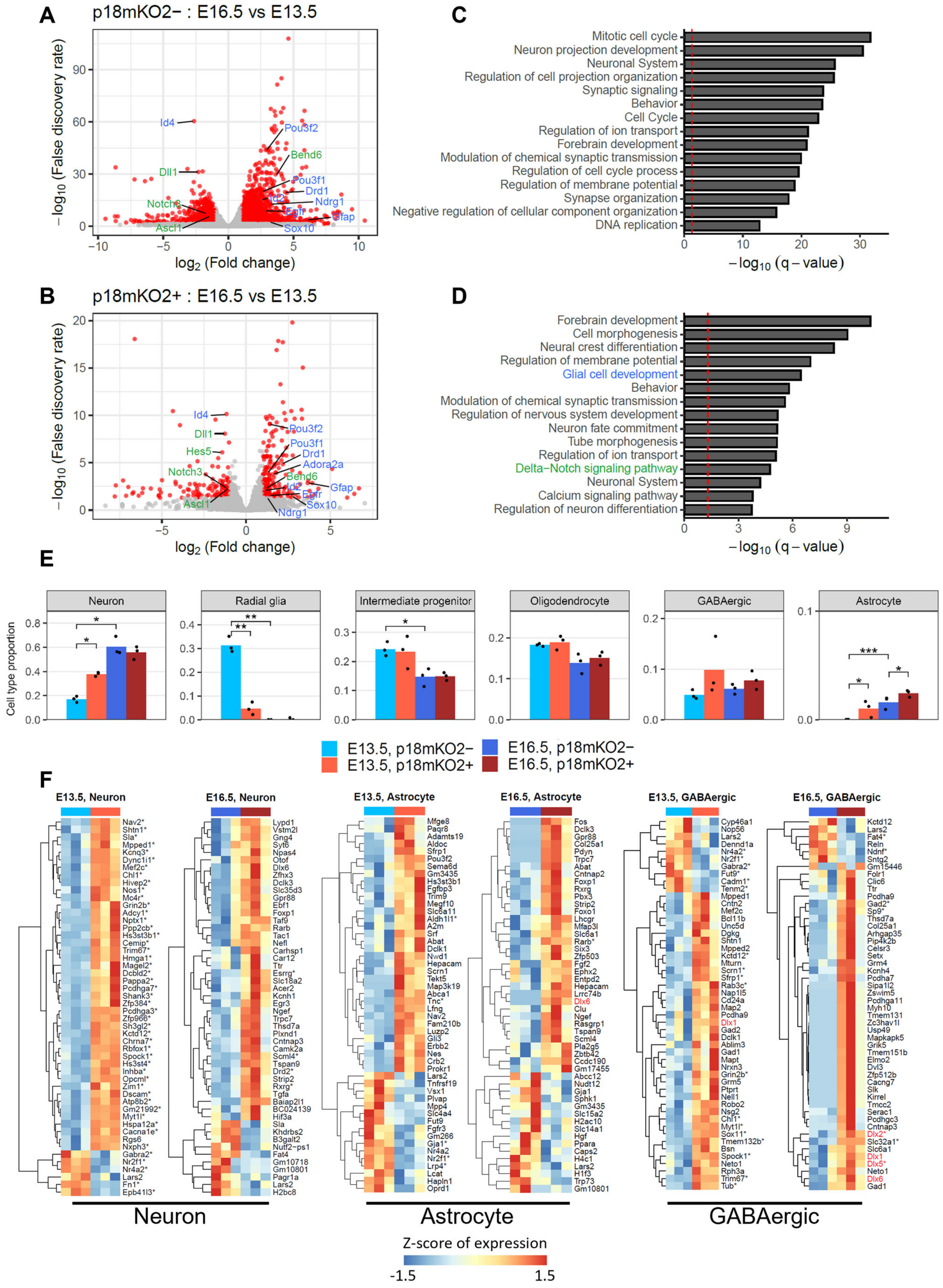
A
p18mKO2− : E16.5 vs E13.5
−log10 (False discovery rate)
log2 (Fold change)
Id4
Pou3f2
Bend6
Dll1
Pou3f1
Drd1
Id2
Ndrg1
Notch3
Egfr
Gfap
Ascl1
Sox10
B
p18mKO2+ : E16.5 vs E13.5
Hes5
Adora2a
C
Mitotic cell cycle
Neuron projection development
Neuronal System
Regulation of cell projection organization
Synaptic signaling
Behavior
Cell Cycle
Regulation of ion transport
Forebrain development
Modulation of chemical synaptic transmission
Regulation of cell cycle process
Regulation of membrane potential
Synapse organization
Negative regulation of cellular component organization
DNA replication
−log10 (q − value)
D
Forebrain development
Cell morphogenesis
Neural crest differentiation
Regulation of membrane potential
Glial cell development
Behavior
Modulation of chemical synaptic transmission
Regulation of nervous system development
Neuron fate commitment
Tube morphogenesis
Regulation of ion transport
Delta−Notch signaling pathway
Neuronal System
Calcium signaling pathway
Regulation of neuron differentiation
E
Cell type proportion
Neuron
Radial glia
Intermediate progenitor
Oligodendrocyte
GABAergic
Astrocyte
E13.5, p18mKO2−
E13.5, p18mKO2+
E16.5, p18mKO2−
E16.5, p18mKO2+
F
E13.5, Neuron
E16.5, Neuron
E13.5, Astrocyte
E16.5, Astrocyte
E13.5, GABAergic
E16.5, GABAergic
Neuron
Astrocyte
GABAergic
Z-score of expression
-1.5
1.5

Figure 6. Cell type proportion and transcriptomic change by p18 OE.

(**A**, **B**) Volcano plots of RNA-seq for each comparison. Red dots ($n = 2828$ for **A** and $n = 354$ for **B**) indicate that the difference in gene expression is statistically significant (false discovery rate (FDR) < 0.05, |fold change (FC)| > 2). Genes that correspond to the biological pathways indicated in (**D**) are marked by identical colors. (**C**, D) Functional enrichment of differentially expressed genes. The Q-value represents an FDR. (**E**) Cell type proportion estimated by BayesPrism using mouse brain scRNA-seq data as the reference. The significance of the difference was calculated using the relative proportion to endothelial cells. One-tailed *t* test. From top to bottom, left to right, $^{*}P = 0.0276$, $^{*}P = 0.0108$ (Neuron), $^{**}P = 0.000270$, $^{**}P = 0.000690$ (Radial glia), $^{*}P = 0.0478$ (Intermediate progenitor), $^{***}P = 0.0000341$, $^{*}P = 0.00471$, $^{*}P = 0.0280$ (Astrocyte). (**F**) Heatmaps of the gene expression z score from the 50 most variable genes between p18mKO2- and p18mKO2 + . Asterisks indicate that the difference in expression is statistically significant (FDR < 0.05). Source data are available online for this figure.

in vitro organoid models are considerable strategies to address this possibility.

Alternatively, comparative analyses of dissociated single-cell transcriptomes among species would be an informative approach. Recently, scRNAseq profiles focusing on the glial production stage of the developing human brain by combining published datasets and immunohistochemistry have been reported (Yang et al, 2022). In their study, the existence of bMIPCs, which can give rise to astrocytes, oligodendrocytes, and OB interneurons, was confirmed in human cells. In the case of mouse brain development, bMIPCs are derived from RGCs via aMIPCs. In humans, RGCs existing in the VZ (vRGs) produce outer RGCs (oRGs) and truncated RGCs (tRGs). oRGs exclusively produce neurons, while tRGs generate neurons, glial cells, and bMIPCs. Notably, oRGs are more proliferative than tRGs (Nowakowski et al, 2016), indicating that the cell cycle of tRGs is longer than that of oRGs. Therefore, the diversity of progenies from tRGs may correlate to the functional level of CDKIs to determine the different constitutions of neurons and glial cells among species. Further studies of the cell cycle and its regulatory machinery will shed light on the evolutionary differences in brain architectures.

Limitations of the study

In this study, we demonstrated the function of p18 in determining the boundaries among different cellular lineages sequentially arising from NSCs. However, further comprehensive understandings of the dynamics of endogenous CDKIs along the lineage transition require monitoring not only gene expression directly (possibly using live imaging by establishing mouse lines with stably expressing fluorescent reporter) but also proteostasis, as CDKIs are subject to ubiquitination during the cell cycle (Forget et al, 2008).

Methods

Reagents and tools table

Reagent/resource	Reference or source	Identifier or catalog number
Experimental models		
Mouse: *AldH1l1*-EGFP	Mutant Mouse Resource & Research Centers (MMRRC)	Cat #011015-UCD
Mouse: P18-P2A-mKO2	This study (RIKEN Center for Biosystems Dynamics Research)	Accession No. CDB1348K
Mouse: Nestin-CreER^{T2}	Kyoto University	N/A
Mouse: Ai9tdTomato	Korea Brain Research Institute	N/A
Mouse: Emx1-Cre	Jackson Laboratory	Cat #005628
Mouse: ICR	Orient Bio/Core Tech	
Mouse: Neural Stem Cell	Imayoshi et al, 2013	N/A
Human: HEK293T Cell	ATCC	CRL-3216
Recombinant DNA		
pCAGGS	Niwa et al, 1991	N/A
pCAG-NLS-EGFP	Konno et al, 2008	N/A
pCAG-p18	Kosodo et al, 2011	N/A
pCAG-FloxP-EGFP-F	Shitamukai et al, 2011	N/A
pCAG-Cre	Shitamukai et al, 2011	N/A
LacZmiRNA	Kosodo et al, 2011	N/A
HA-HES1	Shimojo et al, 2008/ Kobayashi et al, 2015	N/A
E1-pNgn2-luc-3'UTR	Shimojo et al, 2008/ Kobayashi et al, 2015	N/A
PB-*Gfa2*-EGFP	Hamabe-Horiike et al, 2021	N/A
pCAG-p18 (human)	This paper	N/A
pCAG-H2B-TagRFP	This paper	N/A
pCAG-p18-P2A-mKO2	This paper	N/A
pCAG-p27	This paper	N/A
pCAG-CreER^{T2}	Matsuda and Cepko, 2007	N/A
pCAG-Dlx2	This paper	N/A
Antibodies		
Rabbit anti-AldH1l1 (1:500)	Abcam #ab87117	AB_10712968
Goat anti-TAG-1 (1:50)	DSHB #4D7/TAG1	AB_531775
Rabbit anti-Neurogenin2 (1:200)	CST #13144	AB_2798130
Rabbit anti-GFAP (1:500)	Dako #Z0334	AB_10013382
Mouse anti-S100b (1:500)	Abcam #ab11178	AB_297817
Mouse anti-Satb2 (1:500)	Abcam #ab51502	AB_882455
Rabbit anti-Cux1 (1:500)	Proteintech #11733-1-AP	AB_2086995
Rat anti-Ctip2 (1:200)	Abcam #ab18465	AB_2064130
Rat anti-PECAM (1:500)	BD Pharmingen #550274	AB_393571
Rat anti-PDGFRa (1:500)	Invitrogen #16-1401-82	AB_529483
Rabbit anti-SOX10 (1:500)	CST #89356	AB_2792980

Reagent/resource	Reference or source	Identifier or catalog number
Mouse anti-Dlx2 (1:500)	Santa Cruz #sc-393879	
Rabbit anti-Sox9 (1:500)	Millipore #AB5535	AB_2239761
Rabbit anti-Sp8 (1:500)	Novus #NBP2-49109	
Rabbit anti-$p18^{Ink4c}$ (1:1000)	Santa Cruz #sc-865	AB_2078731
Rabbit anti-$p27^{Kip1}$ (1:1000)	Invitrogen #PA-5-27188	AB_2544664
Donkey anti-Chicken IgG, Alexa Fluor 488 conjugated (1:1000)	Jackson Immuno Research #703-545-155	AB_2340375
Donkey anti-rat IgG, Alexa Fluor 488 conjugated (1:1000)	Invitrogen #A21208	AB_141709
Donkey anti-rabbit IgG, Alexa Fluor 488 conjugated (1:1000)	Invitrogen #A21206	AB_2535792
Donkey anti-mouse IgG, Alexa Fluor 488 conjugated (1:1000)	Invitrogen #A21202	AB_141607
Donkey anti-rat IgG, Alexa Fluor 555 conjugated (1:1000)	Invitrogen #A48270	AB_2896336
Donkey anti-goat IgG, Alexa Fluor 555 conjugated (1:1000)	Invitrogen #A21432	AB_2535853
Donkey anti-rabbit IgG, Alexa Fluor 555 conjugated (1:1000)	Invitrogen #A31572	AB_162543
Donkey anti-mouse IgG, Alexa Fluor 555 conjugated (1:1000)	Invitrogen #A31570	AB_2536180
Donkey anti-rat IgG, Alexa Fluor 647 conjugated (1:1000)	Invitrogen #A78947	AB_2910635
Donkey anti-rabbit IgG, Alexa Fluor 647 conjugated (1:1000)	Invitrogen #A31573	AB_2536183
Donkey anti-mouse IgG, Alexa Fluor 647 conjugated (1:1000)	Invitrogen #A31571	AB_2162542
Oligonucleotides and other sequence-based reagents		
Primers	This paper	N/A
Chemicals, enzymes and other reagents		
5-ethynyl-2′-deoxyuridine (EdU)	Invitrogen	Cat #A10044
Corn oil	Sigma	Cat #C8267
4% Paraformaldehyde	Chembio	Cat #CBPF-9004
Sucrose	Kisanbio	Cat #MB-S4842-1
Bovine Serum Albumin	Sigma	Cat #A9647
Triton X-100	Sigma	Cat #X100
FastStart Universal SYBR Green Master	Roche	Cat #0913850001
Papain	Worthington	Cat #LK003153
Poly-L ornithine	Sigma	Cat #P3655
Fibronectin	R&D Systems	Cat #1030-FN-05M
ViaFect transfection reagent	Promega	Cat #E4982
DMEM/F12	Gibco	Cat #11039-021
Penicillin/streptomycin	Gibco	Cat #15140-122
N2 plus media supplement	R&D Systems	Cat #AR009
Fibroblast Growth Factor (basic) (bFGF)	Wako	Cat #060-04543
Epidermal Growth Factor (EGF)	Invitrogen	Cat #53003-018
B-27 Supplement Minus Vitamin A	Invitrogen	Cat #12587-010
Leukemia Inhibitory Factor (LIF)	Millipore	Cat #ESG1106
Recombinant Human BMP-4 Protein	R&D Systems	Cat #314-BP-010
Fetal Bovine Serum (FBS)	Gibco	Cat #16000-044
Entobar (Sodium Pentobarbital)	Hanlim Pharm	
DMEM with high glucose	Welgene	Cat #LM001-09
PEI-MAX	Polysciences	Cat #24765-1
Opti-MEM	Invitrogen	Cat #31985-062
Software		
NIS-Elements	Nikon Instruments Inc	N/A
Imaris	Oxford Instruments	N/A
Adobe Photoshop	Adobe Systems	N/A
Metamorph	Molecular Devices	N/A
ImageJ	ImageJ	https://imagej.nih/gov/ij
GraphPad Prism 10	GraphPad	https://www.graphpad.com
MATLAB	MathWorks	N/A
Kaluza	Beckman Coulter	N/A
RSEM/STAR	Incodom	https://incodom.kr
DESeq2	Bioconductor	https://bioconductor.org
Metascape	Metascape	https://metascape.org
BayesPrism	BayesPrism	https://bayesprism.org
BioRender	BioRender	https://www.biorender.com
Adobe Illustrator	Adobe Systems	N/A
Other		
Tyramide Signal Amplification Kit	Molecular Probes	Cat #40993
Click-iT EdU imaging Kit	Invitrogen	Cat #C10340
NucleSpin RNA XS	Macherey-Nagel	Cat #740902.50
PureLink Hipure Plasmid Maxiprep Kit	Invitrogen	Cat #K2100-07

Reagent/resource	Reference or source	Identifier or catalog number
ReverTra Ace qPCR RT Kit	TOYOBO	Cat #FSQ-201
Dual-Luciferase Reporter Assay System	Promega	Cat #E1910
MethylEasy™ Xceed Rapid DNA Bisulfite Modification Kit	Genetic Signatures	
NETflex Rapid Directional RNA-Seq Kit	PerkinElmer	Cat #NOVA-5198-10

Methods and protocols

Animals

The *AldH1l1*-EGFP line was imported from Mutant Mouse Resource & Research Centers (MMRRC, USA); the p18-P2A-mKO2 knock-in (KI) mouse line was generated and imported from RIKEN Center for Biosystems Dynamics Research (Japan); the Nestin-CreER^{T2} line (Imayoshi et al, 2006) was kindly provided by Dr. Ryo-ichiro Kageyama (Kyoto Univ, Japan); the Ai9tdTomato line was housed at the KBRI; and the Emx1-Cre line was purchased from the Jackson Laboratory (#005628, USA). Pregnant ICR mice were purchased from Orient Bio or Core Tech (Republic of Korea). The plug date was considered embryonic day (E) 0.5. For the EdU assay, EdU (A10044, Invitrogen) was dissolved in PBS and administered by intraperitoneal (IP) injection at a concentration of 5 mg/kg. Tamoxifen (T5648, Sigma) was dissolved in corn oil (C8267, Sigma) at a concentration of 10 mg/ml, and 2 mg was injected into pregnant mice by IP injection. All experiments were approved by the animal care and use committee of KBRI (IACUC-22-00027) and the Institutional Animal Care and Use Committee of RIKEN Kobe Branch (A2001-03).

Generation of p18-P2A-mKO2 knock-in mice

p18-P2A-mKO2 mice (Accession No. CDB1348K: https://large.riken.jp/distribution/mutant-list.html) were generated by using HK3i embryonic stem (ES) cells derived from C57BL/6 (Kiyonari et al, 2010). The targeting vector was generated with the Gateway system (Thermo Fisher Scientific). In brief, p18-P2A-mKO2 was cloned into the pENTR2B vector (Thermo Fisher Scientific) and inserted into pROSA26-CAG-STOP-DEST, which was modified from pROSA26-STOP-DEST (Abe et al, 2011) and pCAGGS (Niwa et al, 1991). The targeted ES clones were microinjected into 8-cell stage ICR embryos, and the embryos were transferred into pseudopregnant ICR females. The resulting chimeras were bred with C57BL/6 mice, and heterozygous offspring were identified by PCR using the following primers: R26 gt Wt FW2 (P3, 5′-TCC CTC GTG ATC TGC AAC TCC AGT C-3′) and R26 gt Wt REV2 (P4, 5′-AAC CCC AGA TGA CTA CCT ATC CTC C-3′) for the wild-type allele (217 bp), and bpA FW (P7, 5′-GGG GGA GGA TTG GGA AGA CAA TAG C-3′) and R26 gt Wt REV2 for the R26R allele (297 bp). R26 FloxP CAG FW (5′-TCC TGG GCA ACG TGC TGG-3′) and R26 gt Mt FloxP REV (P5, 5′-TGT GGA ATG TGT GCG AGG CCA GAG G-3′) for the R26 allele (217 bp), R26 FloxP CAG FW and R26 gt Mt dloxP REV (P6, 5′-GCT GCA GGT CGA GGG ACC-3′) for the R26 allele (113 bp).

Immunostaining and imaging

Brain tissues were fixed overnight in 4% paraformaldehyde at 4 °C before cryoprotection with 20% sucrose. Brains were then embedded in OCT compound for cryosectioning. After culturing in a proliferative or astrocyte induction medium, NS cells were fixed in 4% paraformaldehyde for 10 min. Frozen sections (15 μm thickness) or fixed NS cells were incubated in blocking solution (2% bovine serum albumin and 0.1% Triton X-100 in PBS), then overnight with primary antibodies (rabbit anti-AldH1l1 (1:500; #ab87117, Abcam), goat anti-TAG-1 (1:50; #4D7/TAG1, DSHB), rabbit anti-Neurogenin2 (1:200; #13144, CST), rabbit anti-GFAP (1:500; #Z0334, Dako), mouse anti-S100b (1:500; #ab11178, Abcam), mouse anti-Satb2 (1:500; #ab51502, Abcam), rabbit anti-Cux1 (1:500; #11733-1-AP, Proteintech), rat anti-Ctip2 (1:200; #ab18465, Abcam), rat anti-PECAM (1:500; #550274, BD Pharmingen), rat anti-PDGFRa (1:500; #16-1401-82, Invitrogen), rabbit anti-SOX10 (1:500; #89356, CST), mouse anti-Dlx2 (1:500; #sc-393879, Santa Cruz), rabbit anti-Sox9 (1:500; #AB5535, Millipore), or rabbit anti-Sp8 (1:500; #NBP2-49109, Novus) and counterstained with 4,6-di-amino-2-phenyl-indole dihydrochloride (DAPI). Alexa 488, 555, and 647 nm conjugated secondary antibodies (1:1000; Molecular Probes) were then applied. To confirm p18 or p27 expression in brain tissue, rabbit anti-p18^{Ink4c} (1:1000; #sc-865, Santa Cruz) or rabbit anti-p27^{Kip1} (1:1000; #PA-5-27188, Invitrogen) was used, and the signal was amplified by biotin-XX-labeled tyramides (Tyramide Signal Amplification Kits; #40993, Molecular Probes). To confirm cell cycle arrest, EdU was detected using Click-iT EdU imaging kits (#C10340, Invitrogen). Briefly, sections were incubated overnight with primary antibody against EGFP to detect the electroporated cells by immunostaining. EdU detection was carried out before the secondary antibody reaction.

Samples were observed using a confocal laser microscope (Ti-RCP, Nikon and Dragonfly 502w, Andor Technology), and composite images were created using Adobe Photoshop software (Adobe Systems). Image quantifications were performed using Metamorph or ImageJ software; we first marked the number of electroporated cells per image under a 20× or 40× objective lens and then counted double-positive cell populations. Cell numbers were averaged, statistical analyses were performed, and the results are shown in a graph generated by Prism software. The total counted cell number for each condition is displayed in italics in the figure legends. The threshold and image calculator functions of ImageJ were used to quantify the overlap of immunostaining signals.

Laser microdissection

Brain tissues were collected from E13.5 to E17.5 of *AldH1l1*-EGFP mice or E13.5 and E16.5 of NestinCreER^{T2}/p18mKO2 mice and then embedded in OCT compound without fixation. Fresh frozen tissue was cryosectioned at 30 μm thickness and then fixed with ice-cold 70% ethanol for 1 min. Sections washed with RNase-free water to remove OCT compound were dissected using laser microdissection microscopy (PALM MicroBeam with Axio Observer Z1, Zeiss) to collect only the ventricular surface of dorsal cortexes. Ten to 12 pieces of tissue were collected, and total mRNA was extracted to investigate p18, p27, and EGFP expression levels in *AldH1l1*-EGFP mice and bulk RNA-seq in NestinCreER^{T2}/p18mKO2 mice. Total mRNA was isolated using NucleoSpin RNA XS (#740902.50, Macherey-Nagel) and then applied to TapeStation 4200 (Agilent) to examine quality and measure concentrations.

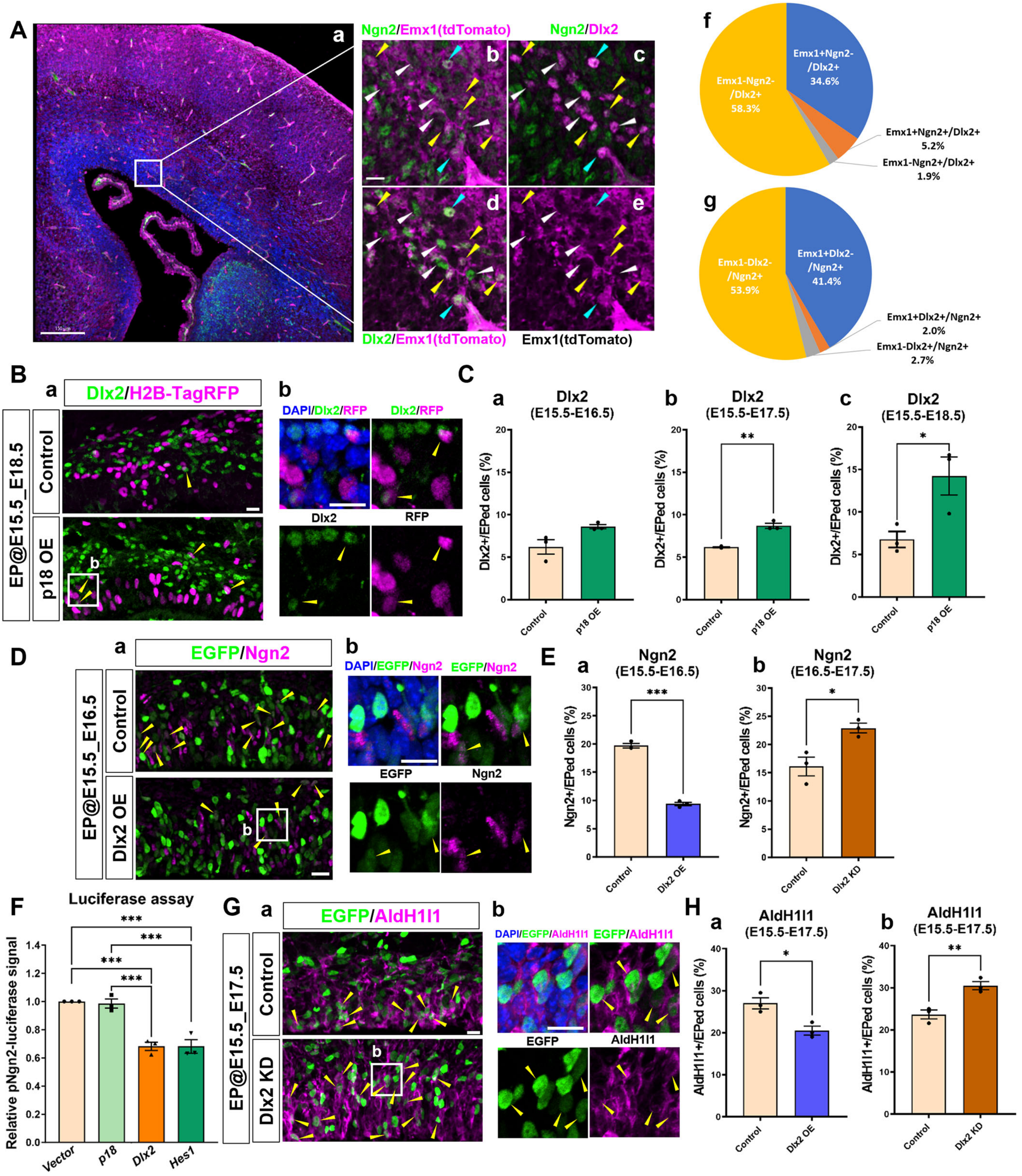

Plasmids

Plasmids were constructed according to standard protocols for DNA cloning. Prior to electroporation into mouse brain tissue or transfection into cultured cells, plasmids were purified with the PureLink HiPure Plasmid Maxiprep Kit (#K2100-07, Invitrogen). The following plasmids were constructed in previous studies: pCAGGS (Niwa et al, 1991); pCAG-NLS-EGFP (Konno et al, 2008); pCAG-p18 (Kosodo et al, 2011); pCAG-FloxP-EGFP-F and pCAG-Cre (Shitamukai et al, 2011); and LacZmiRNA (Kosodo et al, 2011).

Figure 7. Expression of Dlx2 and its function in the dorsal cortex.

(**A**) (a) Images of E17.5 Emx1-Cre/Ai9 mouse brains stained with Ngn2 and Dlx2 antibodies. Bar, 150 μm. (b–e) Magnified view of the square region in (a). Arrowheads; blue, Dlx2 + /Ngn2 + /tdTomato + ; yellow, Dlx2 + /Ngn2-/tdTomato + ; white, Dlx2 + /tdTomato-. Bar, 15 μm. (f, g) Quantification of the stained images (*n* = 4 brains each). Total counted cells of Dlx2 + , Ngn2 + ; *311, 282*. (**B**) Plasmids to induce OE of p18 mixed with pCAG-H2B-TagRFP were delivered at E15.5 and then fixed after 1–3 d. Sections were stained using Dlx2 antibody. (a) Images of fixation at E18.5 are presented. Arrowheads; double-positive cells to Dlx2 and H2B-TagRFP. Bar, 30 μm. (b) Magnified view of the square region in (a). Arrowheads; double-positive cells to Dlx2 and H2B-TagRFP. Bar, 10 μm. (**C**) Quantification of the Dlx2-positive cells among EGFP-positive cells in (**B**) (*n* = 3 brains each). Total counted cells of Control, p18 OE; *410, 549* (E16.5); *453, 413* (E17.5); *309, 167* (E18.5). Two-tailed *t* test; error bars show mean ± SEM. $^{**}P = 0.00118109$ (b), $^{*}P = 0.03660486$ (c). (**D**) Plasmids to induce OE and KD of Dlx2 mixed with pCAG-NLS-EGFP were delivered at E15.5 and 16.5, respectively, and then fixed after 1 d. Sections were stained using Ngn2 antibody. (a) Images of IUE at E15.5 for Dlx2 OE are presented. Arrowheads; double-positive cells for Ngn2 and EGFP. Bar, 30 μm. (b) Magnified view of the square region in (a). Arrowheads; double-positive cells to Ngn2 and EGFP. Bar, 10 μm. (**E**) Quantification of the Ngn2-positive cells among EGFP-positive cells in (**D**) (*n* = 3 brains each). Total counted cells of Control, Dlx2 OE; *337, 438*; Control, Dlx2 KD; *425, 322*. Two-tailed *t* test; error bars show mean ± SEM. $^{***}P = 0.00003530$ (a), $^{*}p = 0.03660486$ (b). (**F**) Luciferase assay using the promoter region of Ngn2 in HEK293T cells transfected with plasmids to induce p18, Dlx2, and Hes1 expression (*n* = 3 independent cultures). One-way ANOVA with Tukey's test; error bars show mean ± SEM. From top to bottom, $^{***}P = 0.00049901$, $^{***}P = 0.00069031$, $^{***}P = 0.00051001$, $^{***}P = 0.00070606$. (**G**) Plasmids to induce OE and KD of Dlx2 mixed with pCAG-NLS-EGFP were delivered at E15.5 and then fixed at E17.5. Sections were stained using AldH1l1 antibody. (a) Arrowheads; double-positive cells for AldH1l1 and EGFP. Bar, 30 μm. (b) Magnified view of the square region in (a). Arrowheads; double-positive cells to AldH1l1 and EGFP. Bar, 10 μm. (**H**) Quantification of the AldH1l1-positive cells among EGFP-positive cells in (**G**) (*n* = 3 brains each). Total counted cells of Control, Dlx2 OE; *515, 468*; Control, Dlx2 KD; *649, 581*. Two-tailed *t* test; error bars show mean ± SEM. $^{*}P = 0.01812292$ (a), $^{**}P = 0.00895741$ (b). Source data are available online for this figure.

HA-HES1 and E1-pNgn2-luc-3′UTR were constructed in previous works (Kobayashi et al, 2015; Shimojo et al, 2008). PB-*Gfa2*-EGFP (Hamabe-Horiike et al, 2021) was used with the PiggyBac Transposon Vector System (#PB210 and #PB512, System Bioscience) for the transposon-based fluorescent reporter assay. To generate pCAG-p18 (human), a full-length human *P18* coding sequence was amplified from human iPSC-derived cDNA using PCR and ligated into pCAGGS. To generate pCAG-H2B-TagRFP, the TagRFP coding sequence from pTagRFP-N (#FP142, Evrogen) was inserted into pCAG-H2B-EGFP (Konno et al, 2008) by replacing EGFP using BamH1 and Not1. To generate pCAG-p18-P2A-mKO2, first, the p18 coding sequence was ligated into pCAG-EGFP-N1 (Konno et al, 2008). Then, the mKO2 coding sequence amplified from pmKO2-S1 (#AM-V0141M, MBL) using primers containing the P2A sequence (Kim et al, 2011) was inserted by replacing EGFP using BamH1 and Not1. To generate pCAG-p27, a full-length mouse p27 coding sequence was amplified from embryonic mouse brain-derived cDNA and ligated into pCAG-CreER^{T2} (Matsuda and Cepko, 2007) using EcoR1 and Not1. To generate pCAG-Dlx2, the full-length mouse Dlx2 coding sequence was amplified from embryonic mouse brain-derived cDNA and ligated into pCAG-EGFP-N1 using EcoR1 and Not1. To generate KD constructs for p18, p27, and Dlx2, the BLOCK-iT Pol II miR RNAi Expression Vector Kit (#K4935-00, Invitrogen) was used with the listed oligos as described in a previous study (Kosodo et al, 2011). To generate shRNA constructs for p18 and p27, pSilencer 3.0-H1 (#V012700, NovoPro) was used with the listed oligos. Briefly, oligonucleotides corresponding to the target coding sequence and its complementary sequence were inserted into the pSilencer 3.0-H1 vector using *Bam*H1 and *Hind*III sites. Primer sequences are provided in Table 1.

Quantitative real-time PCR (qPCR)

The isolated total mRNA was used to synthesize equal amounts of cDNA to quantify specific gene expression using the ReverTra Ace qPCR RT kit (#FSQ-201, TOYOBO). qPCR was performed using FastStart Universal SYBR Green Master (#0913850001, Roche) at 95 °C for 10 min, then 40 cycles of 95 °C for 15 s and 60 °C for 60 s. GAPDH was amplified as an internal control, and the specificity of the reaction was verified by melt curve analysis. Experiments were conducted using a Light Cycler 480II (Roche). Primer sequences used for quantitative real-time PCR are provided in Table 2.

Preparation of NS cells

NS cells were prepared according to a previous publication (Imayoshi et al, 2013) with some modifications. Dorsal cortexes were dissected from EGFP-positive brains of E14.5 *AldH1l1*-EGFP mice and enzymatically dissociated using papain (#LK003153, Worthington) in DMEM/F12 medium. Cells were plated on a 12-well plate coated with 15 μg/ml poly-L ornithine (#P3655, Sigma) and 1 μg/ml fibronectin (#1030-FN-05M, R&D Systems). The cell density was adjusted to 2.5×10^5 cells/well and incubated at a confluence of 50–60% in a 12-well plate for transfection. One microgram of DNA from the mKO2 or p18-2A-mKO2 construct was mixed with 3 μl of ViaFect transfection reagent (#E4982, Promega) for p18-overexpression experiments. The mixture was incubated in NS cell culture medium for 10 h. The cells were washed with PBS, and then proliferative medium (DMEM/F12 (#11039-021, Gibco), 1× penicillin/streptomycin (#15140-122, Gibco), 1× N2 plus media supplement (#AR009, R&D Systems), 20 ng/ml bFGF (#060-04543, Wako), 20 ng/ml EGF (#53003-018, Invitrogen)) or astrocyte induction medium (DMEM/F12, 0.5× penicillin/streptomycin, 1× N2 plus media supplement, 1× B27 (#12587-010, Invitrogen), 80 ng/ml LIF (#ESG1106, Millipore), 80 ng/ml BMP4 (#314-BP-010, R&D Systems), FBS (#16000-044, Gibco)) were added. Cells were fixed for immunostaining after 48 h.

Flow cytometry and cell sorting

Electroporated NS cells were incubated in astrocyte induction medium for 48 h, harvested by centrifugation, and resuspended in PBS. Subsequently, only electroporated (RFP-positive) cells were isolated by an automated cell sorter (MoFlo Astrios, Beckman Coulter) with 555 nm excitation/584 nm emission wavelengths, and total mRNA was extracted for qPCR from the sorted cell populations.

In utero electroporation

Pregnant mice were anesthetized with 10% sodium pentobarbital, and their intrauterine embryos were exposed after cesarean section.

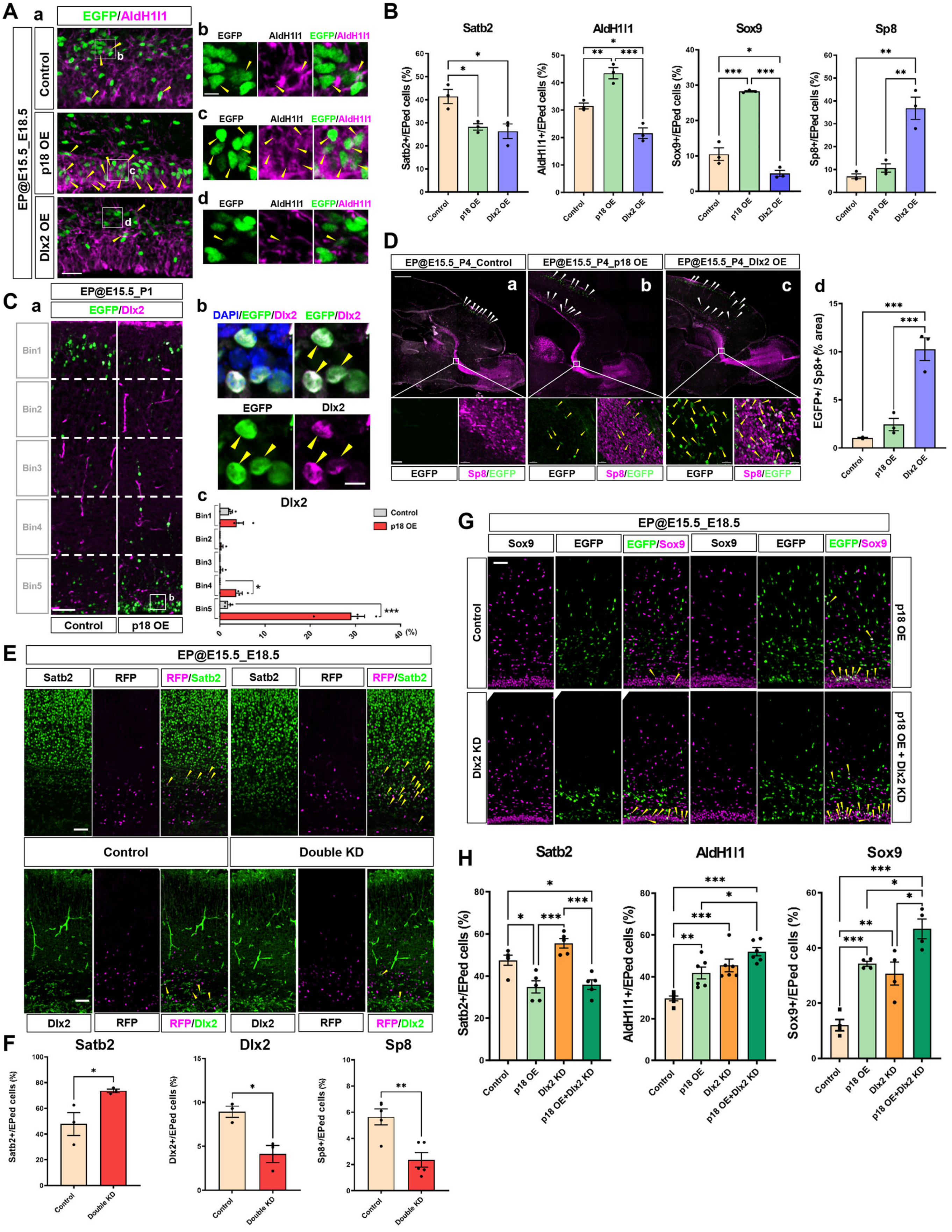
A
a
EGFP/AldH1l1
EP@E15.5_E18.5
Control
p18 OE
Dlx2 OE
b
c
d
EGFP
AldH1l1
EGFP/AldH1l1
B
Satb2
Satb2+/EPed cells (%)
AldH1l1
AldH1l1+/EPed cells (%)
Sox9
Sox9+/EPed cells (%)
Sp8
Sp8+/EPed cells (%)
Control
p18 OE
Dlx2 OE
*
**
***
C
a
EP@E15.5_P1
EGFP/Dlx2
Bin1
Bin2
Bin3
Bin4
Bin5
Control
p18 OE
b
DAPI/EGFP/Dlx2
EGFP/Dlx2
EGFP
Dlx2
c
Dlx2
Control
p18 OE
(%)
D
EP@E15.5_P4_Control
EP@E15.5_P4_p18 OE
EP@E15.5_P4_Dlx2 OE
a
b
c
EGFP
Sp8/EGFP
d
EGFP+/ Sp8+ (% area)
Control
p18 OE
Dlx2 OE
E
EP@E15.5_E18.5
Satb2
RFP
RFP/Satb2
Control
Double KD
Dlx2
RFP
RFP/Dlx2
F
Satb2
Satb2+/EPed cells (%)
Dlx2
Dlx2+/EPed cells (%)
Sp8
Sp8+/EPed cells (%)
Control
Double KD
G
EP@E15.5_E18.5
Sox9
EGFP
EGFP/Sox9
Control
p18 OE
Dlx2 KD
p18 OE + Dlx2 KD
H
Satb2
Satb2+/EPed cells (%)
AldH1l1
AldH1l1+/EPed cells (%)
Sox9
Sox9+/EPed cells (%)
Control
p18 OE
Dlx2 KD
p18 OE+Dlx2 KD

Figure 8. Lineage transitions of UL neurons, astrocytes, and OB interneurons.

(**A**) Plasmids to induce OE of p18 and Dlx2 mixed with pCAG-NLS-EGFP were delivered at E15.5 and then fixed at E18.5. Sections were stained using Satb2, AldH1l1, Sox9, and Sp8 antibodies. (a) Images of staining with AldH1l1 are presented. Bar, 50 μm. (b–d) Magnified view of the square region in (a). Bar, 10 μm. Arrowheads; double-positive cells for AldH1l1 and EGFP. (**B**) Quantification of the Satb2-, AldH1l1-, Sox9-, and Sp8-positive cells among EGFP-positive cells in (**A**) ($n = 3$ brains each). Total counted cells of Control, p18 OE, Dlx2 OE; *283, 261, 380* (Satb2, SP8); *324, 256, 328* (AldH1l1); *340, 249, 265* (Sox9). One-way ANOVA with Tukey's test; error bars show mean ± SEM. From top to bottom, left to right, *$P = 0.02873290$, *$P = 0.01608185$ (Satb2), *$P = 0.01522693$, **$P = 0.00652441$, ***$P = 0.00026211$ (AldH1l1), *$P = 0.03799166$, ***$P = 0.00009784$, ***$P = 0.00002040$ (Sox9), **$P = 0.00113463$, **$P = 0.00226063$ (Sp8). (**C**) (a) Plasmids to induce OE of p18 mixed with pCAG-NLS-EGFP were delivered at E15.5, followed by fixation at P1. Sections were stained using Dlx2 antibody. Bar, 100 μm. Arrowheads; double-positive cells for Dlx2 and EGFP. (b) Magnified view of the square region in (a). Bar, 10 μm. (**c**) The bars indicate the proportions of Dlx2-positive cells among electroporated cells in each BIN. *t* tests were performed between the control and p18 OE in the same BINs ($n = 3$ brains each). Total counted cells of Control, p18 OE; *295, 246*. Two-tailed *t* test; error bars show mean ± SEM. From top to bottom, *$P = 0.01566438$, ***$P = 0.00004670$. (**D**) (a–c) Plasmids to induce OE of p18 and Dlx2 were delivered under the same conditions as C and then fixed at P4. Sections were stained using Sp8 antibody to detect RMS (magnified in the bottom). White arrowheads; EGFP + /Sp8- cells. Yellow arrowheads; EGFP + /Sp8+ cells. Bars in low and high magnified view, 500 and 20 μm, respectively. (d) Quantification of the EGFP-positive area in (a–c) ($n = 3$ brains each, normalized by the Sp8-positive area). One-way ANOVA with Tukey's test; error bars show mean ± SEM. From top to bottom, ***$P = 0.00092368$, ***$P = 0.00037638$. (**E**) Plasmids to induce KD of p18 and p27 mixed with pCAG-H2B-TagRFP were delivered at E15.5 and then fixed at E18.5. Sections were stained using Satb2, Dlx2, and Sp8 antibodies. Images of staining with Satb2 and Dlx2 are presented. Arrowheads; double-positive cells for Satb2/Dlx2 and EGFP. Bar, 100 μm. (**F**) Quantification of Satb2-, Dlx2-, and Sp8-positive cells among H2B-TagRFP-positive cells in (**E**) ($n = 3$–5 sections from 3 brains each). Total counted cells of Control, p18/p27 KD; *179, 159* (Satb2); *188, 237* (Dlx2); 428*, 376* (SP8). Two-tailed *t* test; error bars show mean ± SEM. *$P = 0.04605735$ (Satb2), *$P = 0.01445994$ (Dlx2), **$P = 0.00401234$ (Sp8). (**G**) Plasmids to induce OE of p18 and KD of Dlx2 mixed with pCAG-NLS-EGFP were delivered at E15.5 and then fixed at E18.5. Sections were stained using Satb2, AldH1l1, and Sox9 antibodies. Images of staining with Sox9 are presented. Arrowheads; double-positive cells for Sox9 and EGFP. Bar, 100 μm. (**H**) Quantification of Satb2-, AldH1l1-, and Sox9-positive cells among EGFP-positive cells ($n = 4$–6 sections from 3 brains each). Total counted cells of Control, p18 OE, Dlx2 KD, p18 OE with Dlx2 KD; 449*, 326, 280, 272* (Satb2); *345, 262, 222, 236* (AldH1l1); 411*, 432, 331, 394* (Sox9). One-way ANOVA with Tukey's test; error bars show mean ± SEM. From top to bottom, left to right, *$P = 0.02158542$, *$P = 0.01150958$, ***$P = 0.00012278$, ***$P = 0.00022252$ (Satb2), ***$P = 0.00001046$, *$P = 0.03252156$, ***$P = 0.00077312$, **$P = 0.00848468$ (AldH1l1), ***$P = 00001319$, *$P = 0.04602633$, *$p = 0.01037045$, **$P = 0.00386438$, ***$P = 0.00094264$ (Sox9). Source data are available online for this figure.

Approximately 1 μl of the plasmid solution containing 0.01% fast green was injected into the brain ventricle using a mouth-controlled micropipette. Electronic pulses (40 V, 50 ms, 950-ms intervals, 4 times) were then applied using an electroporator (NEPA21, NEPAGENE). The concentrations of the plasmid were as follows: 1.0 μg/μl pCAG-p18, pCAG-p27, pCAG-Dlx2, and pCAG-empty vector (for negative control); 0.5 μg/μl pCAG-H2B-TagRFP for overexpression; 1.0 μg/μl miR p18, miR p27, miR Dlx2, and miR LacZ (for negative control); 0.5 μg/μl pCAG-H2B-TagRFP and pCAG-NLS-EGFP for knockdown; and 1.0 μg/μl PB-Gfa2-EGFP, PB-RFP, and 0.5 μg/μl PB Transposase. All plasmids were delivered to the dorsal cortex.

Luciferase assay

A luciferase assay was performed using the Dual-Luciferase Reporter Assay System (#E1910, Promega) according to the company's instructions. Briefly, HEK293T cells were cultured in DMEM with high glucose (#LM 001-09, Welgene), 10% FBS, and 1× penicillin/streptomycin. Plasmids were transfected using PEI-MAX (#24765-1, Polysciences) in Opti-MEM (#31985-062, Invitrogen). For normalization, pRL-TK plasmids (Promega) were cotransfected. After 24 h of culture, cell lysates were prepared using a Passive Lysis Buffer kit. Luciferase Assay Buffer II and Stop and Glo Substrate were applied sequentially during the quantification of luminescent signals using a FlexStation 3 microplate reader system (Molecular Probes).

DNA methylation analysis

After making fresh frozen sections using NestinCreER^{T2}/p18mKO2 E13.5 and E16.5 mouse embryonic brains treated with tamoxifen at E12.5 and E15.5, respectively, the target area, including the ventricular zone, was dissected and collected using laser microdissection. Their genomic DNA was extracted using the NucleoSpin Tissue XS kit. Sodium bisulfite treatment of genomic DNA was performed using the MethylEasy^{TM} Xceed Rapid DNA Bisulfite Modification Kit (Genetic Signatures). The region of the bisulfite-treated Gfap promoter (Takizawa et al, 2001) was amplified by PCR using the following primers: GFAP_Tak_F2 (5′-GTATAGATATAATGGTTAGGGGTG-3′) and GFAP_Tak_R (5′-TCTACCCATACTTAAACTTCTAATATCTAC-3′). The PCR products were cloned into a TA cloning vector (RBC Bioscience Corp.), and 10-12 randomly picked from each of 3–4 independent PCR amplifications from different mouse brains were sequenced.

Morphological analysis of 3D-reconstructed cells

To visualize the single-cell morphology, we used a sparse expression vector system described previously (Shitamukai et al, 2011). Embryonic brains were coelectroporated with pCAG-FloxP-EGFP-F (0.5 μg/μl) and a low concentration of Cre recombinase expression vector (10 ng/μl) with 0.5 μg/μl pCAG-H2B-TagRFP, which resulted in high and sparse expression of fluorescent reporters labeling the cellular membrane and nuclear position by EGFP and TagRFP, respectively. Electroporated brains were dissected at the P10 stage and fixed overnight in 4% paraformaldehyde. The fixed brains were embedded in 2% agarose in PBS and solidified on ice. The agarose block containing the brain was then glued to a metal mounting block and sectioned at 200 μm thickness using a vibratome (VT1200S, Leica). Images of sparsely labeled electroporated cells in the brain were acquired using an inverted confocal microscope (Ti-RCP, Nikon). A 20x objective lens (NA = 0.75) was used with a zoom factor of 6.410. Fifty-micron z-stack sections were acquired with a 0.6 μm interval between each optical section.

Subsequently, stacked images were subjected to quantitative morphological analysis using MATLAB, performed by another examiner without knowing the contents of electroporated plasmids (blind test). To quantify nuclear volume, a signal of the RFP channel was extracted and analyzed. A median and average filter was applied (3 × 3 × 3). Subsequently, binarization was performed

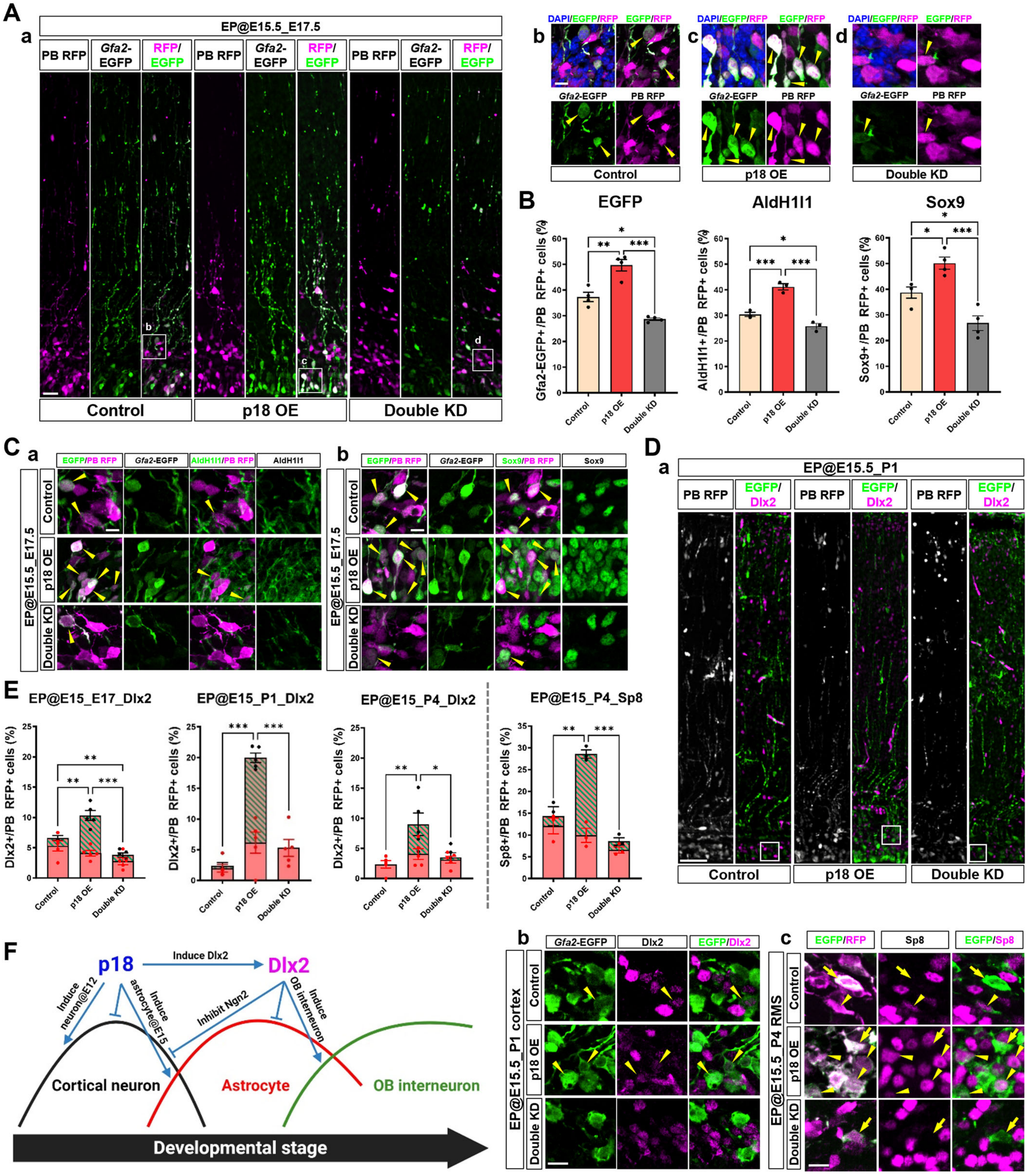
A
a
EP@E15.5_E17.5
PB RFP
Gfa2-EGFP
RFP/EGFP
Control
p18 OE
Double KD
b
c
d
DAPI/EGFP/RFP
EGFP/RFP
Gfa2-EGFP
PB RFP
B
EGFP
AldH1l1
Sox9
Gfa2-EGFP+/PB RFP+ cells (%)
AldH1l1+/PB RFP+ cells (%)
Sox9+/PB RFP+ cells (%)
C
EP@E15.5_E17.5
EGFP/PB RFP
AldH1l1/PB RFP
AldH1l1
Sox9/PB RFP
Sox9
D
EP@E15.5_P1
EGFP/Dlx2
E
EP@E15_E17_Dlx2
EP@E15_P1_Dlx2
EP@E15_P4_Dlx2
EP@E15_P4_Sp8
Dlx2+/PB RFP+ cells (%)
Sp8+/PB RFP+ cells (%)
F
p18
Induce Dlx2
Dlx2
Induce neuron@E12
Induce astrocyte@E15
Inhibit Ngn2
Induce OB interneuron
Cortical neuron
Astrocyte
OB interneuron
Developmental stage
EP@E15.5_P1 cortex
Dlx2
EGFP/RFP
Sp8
EGFP/Sp8
EP@E15.5_P4 RMS

using the threshold of 50% of the signal-to-noise ratio. Finally, the centroid position (Xc, Yc, and Zc) was calculated. For the analysis of the cellular process occupied area, a signal of the EGFP channel projected to the XY-plane was extracted. Averaging and binarization were performed as indicated for the RFP channel. Blank among processes was filled after maximum intensity projection. The farthest position from the centroid (Xc, Yc, and Zc) in the projected area was identified. The image field was rotated to fit the point on the y-axis, and then the projected area was subdivided into 8 orientations. Based on this image processing, the length of the

◀ **Figure 9. Investigation of the lineage transitions at the single-cell level.**

(**A**) (a) Plasmids to induce OE of p18 and double KD of p18/p27 mixed with PB-*Gfa2*-EGFP, PB-RFP, and PBase were delivered at E15.5 and then fixed at E17.5. Sections were stained using AldH1l1 or Sox9 antibody. Images of EGFP and RFP are presented. Bar, 30 µm. (b–d) Magnified view of the square region in (a). Arrowheads; double-positive cells for EGFP and RFP. Bar, 10 µm. (**B**) Quantification of EGFP-, AldH1l1-, and Sox9-positive cells among RFP-positive cells ($n = 3$–4 sections from 3 brains each). Total counted cells of Control, p18 OE, Double KD; *234, 298, 349* (EGFP and Sox9); *146, 177, 207* (AldH1l1). One-way ANOVA with Tukey's test; error bars show mean ± SEM. From top to bottom, left to right, $^{*}P = 0.01406736$, $^{**}P = 0.00152748$, $^{***}P = 0.00002786$ (EGFP), $^{*}P = 0.04733737$, $^{***}P = 0.00086532$, $^{***}P = 0.00011757$ (AldH1l1), $^{*}P = 0.02053167$, $^{*}P = 0.02463277$, $^{***}P = 0.00025819$ (Sox9). (**C**) Images of staining with AldH1l1 (a) and Sox9 (b) antibodies. Arrowheads; double-positive cells for AldH1l1 or Sox9 and RFP. Bar, 10 µm. (**D**) (a) Plasmids to induce OE of p18 and double KD of p18/p27 mixed with PB-*Gfa2*-EGFP, PB-RFP, and PBase were delivered at E15.5 and then fixed at P1. Sections were stained with Dlx2 antibody. Bar, 50 µm. (b) Magnified view of the square region in (a). Arrowheads; double-positive cells for EGFP and Dlx2. Bar, 10 µm. (c) Images of the RMS at P4 stained with Sp8 antibody. Arrowheads; double-positive cells for EGFP and Sp8. Arrows; EGFP-positive and Sp8-negative cells. Bar, 10 µm. (**E**) Quantification of Dlx2-positive cells in the cortex and Sp8-positive cells in the RMS among RFP-positive cells ($n = 3$–4 sections from 3 brains each). Each bar is split into *Gfa2*-EGFP-positive (striped area) and -negative (solid area) cells. Total counted cells of Control, p18 OE, Double KD; *280, 342, 409* (Dlx2, E17.5); *410, 343, 309* (Dlx2, P1); *200, 270, 327* (Dlx2, P4); *181, 191, 178* (Sp8, P4). One-way ANOVA with Tukey's test; error bars show mean ± SEM. From top to bottom, left to right, $^{**}P = 0.00964913$, $^{**}P = 0.00150298$, $^{***}P = 0.00000773$ (E17.5, Dlx2), $^{***}P = 0.00000006$, $^{***}P = 0.00000044$ (P1, Dlx2), $^{**}P = 0.00616579$, $^{*}P = 0.02057649$ (P4, Dlx2), $^{**}P = 0.00108087$, $^{***}P = 0.00016285$ (P4, Sp8). (**F**) Schematics of the lineage transition regulated by p18. Source data are available online for this figure.

Table 1. Primers for plasmids generated in this study.

Construct	Primer name	Sequences
pCAG-p18 (human)	p18_Human EcoA2nd	GGGAATTCCACCATGGCCGAGCCTTGGGGG
	p18_Human BamB2nd	CCGGATCCTTATTGAAGATTTGTGGCTCCCCC
pCAG-p18-P2A-mKO2	N1p18EcoA	GGGAATTCCACCATGGCCGAGCCTTG
	N1p18BamB	CCGGATCCTGCAGGCTTGTGGCTCCC
	P2AmKO2N1BamH1A	CCGGATCCAGGAAGCGGAGCTACTAACTTCAGCCTGCTGAAGCAGGCTGGAGACGTGGAGGAGAACCCT GGACCTATGGTGAGTGTGATTAAACC
	P2AmKO2N1Not1B	GGGCGGCCGCTTAGGAATGAGCTACTGCATC
pCAG-p27	p27_mouse EcoA	GGGAATTCACCATGTCAAACGTGAGAGTGTCTAACGG
	p27_mouse Not1B	CCGCGGCCGCTTACGTCTGGCGTCGAAGGCC
pCAG-Dlx2	mDlx2_EcoA	CCGAATTCAGGATGACTGGAGTCTTTGACAG
	mDlx2_Stop_Not1B	CCGCGGCCGCTTAGAAAATCGTCCCCGCGCTC
p18 miRNA	p18_816Top	TGCTGAAACAAAGCGAAAGGAAACCCGTTTTGGCCACTGACTGACGGGTTTCCTCGCTTTGTTT
	p18_816Bot	CCTGAAACAAAGCGAGGAAACCCGTCAGTCAGTGGCCAAAACGGGTTTCCTTTCGCTTTGTTTC
p27 miRNA	p27_1449_TOP	TGCTGACAAATTGAAGCAAGTTCTTCGTTTTGGCCACTGACTGACGAAGAACTCTTCAATTTGT
	p27_1449_BOT	CCTGACAAATTGAAGAGTTCTTCGTCAGTCAGTGGCCAAAACGAAGAACTTGCTTCAATTTGTC
Dlx2 miRNA	Dlx2_986A	TGCTGTTCCACATCTTCTTGAACTTGGTTTTGGCCACTGACTGACCAAGTTCAAAGATGTGGAA
	Dlx2_986B	CCTGTTCCACATCTTTGAACTTGGTCAGTCAGTGGCCAAAACCAAGTTCAAGAAGATGTGGAAC
p18 shRNA	816 A #1	GATCCGGTTTCCTTTCGCTTTGTTTCAAGAGAAACAAAGCGAAAGGAAACCTTTTTTGGAAA
	890 A #2	GATCCAGTTTATGAAATATTTAAATTCAAGAGATTTAAATATTTCATAAACTTTTTTTGGAAA
	925 A #3	GATCCAAAATTCTGATTTCTAACATTCAAGAGATGTTAGAAATCAGAATTTTTTTTTTGGAAA
	942 A #4	GATCCCATGTAATAGCTATTCCTTTTCAAGAGAAAGGAATAGCTATTACATGTTTTTTGGAAA
p27 shRNA	1449 A #1	GATCCAGAACTTGCTTCAATTTGTTTCAAGAGAACAAATTGAAGCAAGTTCTTTTTTTGGAAA
	1844A #2	GATCCGAAAAATTCTTATTTCTTTTTCAAGAGAAAAGAAATAAGAATTTTTCTTTTTTGGAAA
	1907A #3	GATCCGTCTGTAACTTTACACAAATTCAAGAGATTTGTGTAAAGTTACAGACTTTTTTGGAAA
	2375A #4	GATCCGAAAACTTCCGTAGTTATTTTCAAGAGAAATAACTACGGAAGTTTTCTTTTTTGGAAA

longest process and cellular process area projected to the XY-plane were calculated. For the analysis of the cellular process number, a signal of the EGFP channel was treated by a Gaussian filter to enhance the process structure. After binarization using the threshold set to 50% of the signal-to-noise ratio, line extraction was performed in three-dimensional volume. Subsequently, projection to the XY plane, image field rotation, and area division into 8 orientations were conducted. Based on this image processing, the number and density of processes were calculated. Sholl analysis was further performed for the projected image to count the number of

Table 2. Primers for quantitative real-time PCR.

Gene	Primer	Sequences
GAPDH	Forward	CACTCACGGCAAATTCAACGG
	Reverse	ACTCCACGACATACTCAGCACC
EGFP	Forward	AGGACGACGGCAACTACAAGAC
	Reverse	AGTTGTACTCCAGCTTGTGCCC
p18$^{\text{Ink4c}}$	Forward	ATGCTGCCAGAGCAGGTTTC
	Reverse	ACATTGCAGGCTGTGTGCTTC
p27$^{\text{Kip1}}$	Forward	AGCTGAGAGTGTCTAACGGGAG
	Reverse	TTCATGATTGACCGGGCCGAAG
Dlx2	Forward	CGCACCATCTACTCCAGTTTCC
	Reverse	TCTCGCCGCTTTTCCACATC
Neurogenin2	Forward	TGCAGCGCATCAAGAAGACC
	Reverse	GATCTTCGTGAGCTTGGCATCC
AldH1l1	Forward	TCTCCAAATGCCCTACCAGCTC
	Reverse	ACCGCCTTGTCAACATCACTC
GFAP	Forward	GAGAGAGATTCGCACTCAGTA
	Reverse	TGAGGTCTGCAAACTTGGAC
Satb2	Forward	CCAATGTGTCAGCAACCAAG
	Reverse	CTCTCGCTCCACTCTTTCCA

processes across the radius of 6 to 80 μm from the centroid (2 μm steps).

Statistical analysis

Prism (GraphPad Software) was used for statistical analyses. Differences between two groups were analyzed by two-tailed Student's *t* test, and differences between more than two groups were analyzed by ANOVA followed by Tukey's test. Differences were considered significant for *P* values <0.05 (*$P < 0.05$, **$P < 0.01$, and ***$P < 0.001$) unless specifically indicated. All error bars represent the SEM. For qPCR analysis, each point indicates the averaged value of triplicate reactions.

mRNAseq and computational analysis

mRNA-seq was performed on tissue fragments of the VZ in the dorsal cortex cut by LMD. All mRNA-seq libraries were generated using the NEXTflex Rapid Directional RNA-Seq Kit (#NOVA-5198-10, PerkinElmer) with RNA-Seq Barcodes 1–24 beads. The RNA-seq read data were obtained using an Illumina HiSeq 2500.

The adapter sequences were trimmed by cutadapt v3.4. Paired-end reads were aligned to the mouse transcriptome GRCm38 (Ensembl release 100) by STAR v2.7.2b with ENCODE standard options (Dobin et al, 2013). The quantity of aligned read count was estimated by RSEM v1.2.31 (Li and Dewey, 2011). Genes with total read counts less than 10 were excluded from further analysis. The false discovery rate (FDR; Benjamini-Hochberg procedure) from differential expression analysis for each gene was calculated by DESeq2-1.30.1 (Love et al, 2014). Differentially expressed genes were defined with the following threshold: fold change >2 and FDR < 0.05. The functional enrichment analysis of differentially expressed genes was performed by Metascape (Zhou et al, 2019).

The single-cell RNA-seq data of the developing mouse dorsal forebrain were collected from previous research (La Manno et al, 2021). Each cell type and subtype were annotated by their marker genes. The deconvolution of each RNA-seq data point was performed by BayesPrism v2.0 using the scRNA-seq count matrix as a reference (Chu et al, 2022).

Data availability

The RNA-seq data set is deposited to Gene Expression Omnibus, GEO database accession number: GSE265784. The source data are available online for this paper. All unique materials generated in this study are available from the lead contact or deposited organizations with a completed materials transfer agreement.

The source data of this paper are collected in the following database record: biostudies:S-SCDT-10_1038-S44318-024-00325-9.

Expanded view data, supplementary information, appendices are available for this paper at https://doi.org/10.1038/s44318-024-00325-9.

Peer review information

A peer review file is available at https://doi.org/10.1038/s44318-024-00325-9

References

Abe T, Kiyonari H, Shioi G, Inoue K, Nakao K, Aizawa S, Fujimori T (2011) Establishment of conditional reporter mouse lines at ROSA26 locus for live cell imaging. Genesis 49:579–590

Achim K, Salminen M, Partanen J (2014) Mechanisms regulating GABAergic neuron development. Cell Mol Life Sci 71:1395–1415

Andreu Z, Khan MA, Gonzalez-Gomez P, Negueruela S, Hortiguela R, San Emeterio J, Ferron SR, Martinez G, Vidal A, Farinas I et al (2015) The cyclin-dependent kinase inhibitor p27 kip1 regulates radial stem cell quiescence and neurogenesis in the adult hippocampus. Stem Cells 33:219–229

Besson A, Dowdy SF, Roberts JM (2008) CDK inhibitors: cell cycle regulators and beyond. Dev Cell 14:159–169

Calegari F, Huttner WB (2003) An inhibition of cyclin-dependent kinases that lengthens, but does not arrest, neuroepithelial cell cycle induces premature neurogenesis. J Cell Sci 116:4947–4955

Caron N, Genin EC, Marlier Q, Verteneuil S, Beukelaers P, Morel L, Hu MG, Hinds PW, Nguyen L, Vandenbosch R et al (2018) Proliferation of hippocampal progenitors relies on p27-dependent regulation of Cdk6 kinase activity. Cell Mol Life Sci 75:3817–3827

Caviness Jr VS, Takahashi T, Nowakowski RS (1999) The G1 restriction point as critical regulator of neocortical neuronogenesis. Neurochem Res 24:497–506

Chu T, Wang Z, Pe'er D, Danko CG (2022) Cell type and gene expression deconvolution with BayesPrism enables Bayesian integrative analysis across bulk and single-cell RNA sequencing in oncology. Nat Cancer 3:505–517

Dalton S (2015) Linking the cell cycle to cell fate decisions. Trends Cell Biol 25:592–600

Dehay C, Kennedy H (2007) Cell-cycle control and cortical development. Nat Rev Neurosci 8:438–450

Ding WY, Huang J, Wang H (2020) Waking up quiescent neural stem cells: molecular mechanisms and implications in neurodevelopmental disorders. PLoS Genet 16:e1008653

Dinh Duong TA, Hoshiba Y, Saito K, Kawasaki K, Ichikawa Y, Matsumoto N, Shinmyo Y, Kawasaki H (2019) FGF signaling directs the cell fate switch from neurons to astrocytes in the developing mouse cerebral cortex. J Neurosci 39:6081–6094

Dobin A, Davis CA, Schlesinger F, Drenkow J, Zaleski C, Jha S, Batut P, Chaisson M, Gingeras TR (2013) STAR: ultrafast universal RNA-seq aligner. Bioinformatics 29:15–21

Fero ML, Rivkin M, Tasch M, Porter P, Carow CE, Firpo E, Polyak K, Tsai LH, Broudy V, Perlmutter RM et al (1996) A syndrome of multiorgan hyperplasia with features of gigantism, tumorigenesis, and female sterility in p27(Kip1)-deficient mice. Cell 85:733–744

Forget A, Ayrault O, den Besten W, Kuo ML, Sherr CJ, Roussel MF (2008) Differential post-transcriptional regulation of two Ink4 proteins, p18 Ink4c and p19 Ink4d. Cell Cycle 7:3737–3746

Franklin DS, Godfrey VL, Lee H, Kovalev GI, Schoonhoven R, Chen-Kiang S, Su L, Xiong Y (1998) CDK inhibitors p18(INK4c) and p27(Kip1) mediate two separate pathways to collaboratively suppress pituitary tumorigenesis. Genes Dev 12:2899–2911

Furutachi S, Matsumoto A, Nakayama KI, Gotoh Y (2013) p57 controls adult neural stem cell quiescence and modulates the pace of lifelong neurogenesis. EMBO J 32:970–981

Furutachi S, Miya H, Watanabe T, Kawai H, Yamasaki N, Harada Y, Imayoshi I, Nelson M, Nakayama KI, Hirabayashi Y et al (2015) Slowly dividing neural progenitors are an embryonic origin of adult neural stem cells. Nat Neurosci 18:657–665

Grison A, Atanasoski S (2020) Cyclins, cyclin-dependent kinases, and cyclin-dependent kinase inhibitors in the mouse nervous system. Mol Neurobiol 57:3206–3218

Grison A, Gaiser C, Bieder A, Baranek C, Atanasoski S (2018) Ablation of cdk4 and cdk6 affects proliferation of basal progenitor cells in the developing dorsal and ventral forebrain. Dev Neurobiol 78:660–670

Guo T, Liu G, Du H, Wen Y, Wei S, Li Z, Tao G, Shang Z, Song X, Zhang Z et al (2019) Dlx1/2 are central and essential components in the transcriptional code for generating olfactory bulb interneurons. Cereb Cortex 29:4831–4849

Hagey DW, Topcic D, Kee N, Reynaud F, Bergsland M, Perlmann T, Muhr J (2020) CYCLIN-B1/2 and -D1 act in opposition to coordinate cortical progenitor self-renewal and lineage commitment. Nat Commun 11:2898

Hamabe-Horiike T, Kawasaki K, Sakashita M, Ishizu C, Yoshizaki T, Harada SI, Ogawa-Ochiai K, Shinmyo Y, Kawasaki H (2021) Glial cell type-specific gene expression in the mouse cerebrum using the piggyBac system and in utero electroporation. Sci Rep 11:4864

Harada Y, Yamada M, Imayoshi I, Kageyama R, Suzuki Y, Kuniya T, Furutachi S, Kawaguchi D, Gotoh Y (2021) Cell cycle arrest determines adult neural stem cell ontogeny by an embryonic Notch-nonoscillatory Hey1 module. Nat Commun 12:6562

Hindley C, Philpott A (2012) Co-ordination of cell cycle and differentiation in the developing nervous system. Biochem J 444:375–382

Imayoshi I, Isomura A, Harima Y, Kawaguchi K, Kori H, Miyachi H, Fujiwara T, Ishidate F, Kageyama R (2013) Oscillatory control of factors determining multipotency and fate in mouse neural progenitors. Science 342:1203–1208

Imayoshi I, Ohtsuka T, Metzger D, Chambon P, Kageyama R (2006) Temporal regulation of Cre recombinase activity in neural stem cells. Genesis 44:233–238

Itoh Y, Masuyama N, Nakayama K, Nakayama KI, Gotoh Y (2007) The cyclin-dependent kinase inhibitors p57 and p27 regulate neuronal migration in the developing mouse neocortex. J Biol Chem 282:390–396

Kang P, Lee HK, Glasgow SM, Finley M, Donti T, Gaber ZB, Graham BH, Foster AE, Novitch BG, Gronostajski RM et al (2012) Sox9 and NFIA coordinate a transcriptional regulatory cascade during the initiation of gliogenesis. Neuron 74:79–94

Kim JH, Lee SR, Li LH, Park HJ, Park JH, Lee KY, Kim MK, Shin BA, Choi SY (2011) High cleavage efficiency of a 2A peptide derived from porcine teschovirus-1 in human cell lines, zebrafish and mice. PLoS ONE 6:e18556

Kiyokawa H, Kineman RD, Manova-Todorova KO, Soares VC, Hoffman ES, Ono M, Khanam D, Hayday AC, Frohman LA, Koff A (1996) Enhanced growth of mice lacking the cyclin-dependent kinase inhibitor function of p27(Kip1). Cell 85:721–732

Kiyonari H, Kaneko M, Abe S, Aizawa S (2010) Three inhibitors of FGF receptor, ERK, and GSK3 establishes germline-competent embryonic stem cells of C57BL/6N mouse strain with high efficiency and stability. Genesis 48:317–327

Kobayashi T, Iwamoto Y, Takashima K, Isomura A, Kosodo Y, Kawakami K, Nishioka T, Kaibuchi K, Kageyama R (2015) Deubiquitinating enzymes regulate Hes1 stability and neuronal differentiation. FEBS J 282:2411–2423

Kohwi M, Petryniak MA, Long JE, Ekker M, Obata K, Yanagawa Y, Rubenstein JL, Alvarez-Buylla A (2007) A subpopulation of olfactory bulb GABAergic interneurons is derived from Emx1- and Dlx5/6-expressing progenitors. J Neurosci 27:6878–6891

Konno D, Shioi G, Shitamukai A, Mori A, Kiyonari H, Miyata T, Matsuzaki F (2008) Neuroepithelial progenitors undergo LGN-dependent planar divisions to maintain self-renewability during mammalian neurogenesis. Nat Cell Biol 10:93–101

Kosodo Y, Suetsugu T, Suda M, Mimori-Kiyosue Y, Toida K, Baba SA, Kimura A, Matsuzaki F (2011) Regulation of interkinetic nuclear migration by cell cycle-coupled active and passive mechanisms in the developing brain. EMBO J 30:1690–1704

Kriegstein A, Alvarez-Buylla A (2009) The glial nature of embryonic and adult neural stem cells. Annu Rev Neurosci 32:149–184

La Manno G, Siletti K, Furlan A, Gyllborg D, Vinsland E, Mossi Albiach A, Mattsson Langseth C, Khven I, Lederer AR, Dratva LM et al (2021) Molecular architecture of the developing mouse brain. Nature 596:92–96

Lange C, Huttner WB, Calegari F (2009) Cdk4/cyclinD1 overexpression in neural stem cells shortens G1, delays neurogenesis, and promotes the generation and expansion of basal progenitors. Cell Stem Cell 5:320–331

Latres E, Malumbres M, Sotillo R, Martin J, Ortega S, Martin-Caballero J, Flores JM, Cordon-Cardo C, Barbacid M (2000) Limited overlapping roles of P15(INK4b) and P18(INK4c) cell cycle inhibitors in proliferation and tumorigenesis. EMBO J 19:3496–3506

Li B, Dewey CN (2011) RSEM: accurate transcript quantification from RNA-Seq data with or without a reference genome. BMC Bioinforma 12:323

Li X, Liu G, Yang L, Li Z, Zhang Z, Xu Z, Cai Y, Du H, Su Z, Wang Z et al (2021) Decoding cortical glial cell development. Neurosci Bull 37:440–460

Li X, Newbern JM, Wu Y, Morgan-Smith M, Zhong J, Charron J, Snider WD (2012) MEK Is a key regulator of gliogenesis in the developing brain. Neuron 75:1035–1050

Love MI, Huber W, Anders S (2014) Moderated estimation of fold change and dispersion for RNA-seq data with DESeq2. Genome Biol 15:550

Mairet-Coello G, Tury A, Van Buskirk E, Robinson K, Genestine M, DiCicco-Bloom E (2012) p57(KIP2) regulates radial glia and intermediate precursor cell cycle dynamics and lower layer neurogenesis in developing cerebral cortex. Development 139:475–487

Matsuda T, Cepko CL (2007) Controlled expression of transgenes introduced by in vivo electroporation. Proc Natl Acad Sci USA 104:1027–1032

Mori T, Tanaka K, Buffo A, Wurst W, Kuhn R, Gotz M (2006) Inducible gene deletion in astroglia and radial glia-a valuable tool for functional and lineage analysis. Glia 54:21–34

Nagao M, Ogata T, Sawada Y, Gotoh Y (2016) Zbtb20 promotes astrocytogenesis during neocortical development. Nat Commun 7:11102

Nakagawa T, Wada Y, Katada S, Kishi Y (2020) Epigenetic regulation for acquiring glial identity by neural stem cells during cortical development. Glia 68:1554–1567

Nakashima K, Wiese S, Yanagisawa M, Arakawa H, Kimura N, Hisatsune T, Yoshida K, Kishimoto T, Sendtner M, Taga T (1999) Developmental requirement of gp130 signaling in neuronal survival and astrocyte differentiation. J Neurosci 19:5429–5434

Nakayama K, Ishida N, Shirane M, Inomata A, Inoue T, Shishido N, Horii I, Loh DY, Nakayama K (1996) Mice lacking p27(Kip1) display increased body size, multiple organ hyperplasia, retinal dysplasia, and pituitary tumors. Cell 85:707–720

Nalepa G, Barnholtz-Sloan J, Enzor R, Dey D, He Y, Gehlhausen JR, Lehmann AS, Park SJ, Yang Y, Yang X et al (2013) The tumor suppressor CDKN3 controls mitosis. J Cell Biol 201:997–1012

Nguyen L, Besson A, Heng JI, Schuurmans C, Teboul L, Parras C, Philpott A, Roberts JM, Guillemot F (2006) p27kip1 independently promotes neuronal differentiation and migration in the cerebral cortex. Genes Dev 20:1511–1524

Niwa H, Yamamura K, Miyazaki J (1991) Efficient selection for high-expression transfectants with a novel eukaryotic vector. Gene 108:193–199

Nowakowski TJ, Pollen AA, Sandoval-Espinosa C, Kriegstein AR (2016) Transformation of the radial glia scaffold demarcates two stages of human cerebral cortex development. Neuron 91:1219–1227

Salomoni P, Calegari F (2010) Cell cycle control of mammalian neural stem cells: putting a speed limit on G1. Trends Cell Biol 20:233–243

Schirripa A, Sexl V, Kollmann K (2022) Cyclin-dependent kinase inhibitors in malignant hematopoiesis. Front Oncol 12:916682

Shimojo H, Ohtsuka T, Kageyama R (2008) Oscillations in notch signaling regulate maintenance of neural progenitors. Neuron 58:52–64

Shitamukai A, Konno D, Matsuzaki F (2011) Oblique radial glial divisions in the developing mouse neocortex induce self-renewing progenitors outside the germinal zone that resemble primate outer subventricular zone progenitors. J Neurosci 31:3683–3695

Takizawa T, Nakashima K, Namihira M, Ochiai W, Uemura A, Yanagisawa M, Fujita N, Nakao M, Taga T (2001) DNA methylation is a critical cell-intrinsic determinant of astrocyte differentiation in the fetal brain. Dev Cell 1:749–758

Taverna E, Gotz M, Huttner WB (2014) The cell biology of neurogenesis: toward an understanding of the development and evolution of the neocortex. Annu Rev Cell Dev Biol 30:465–502

Tiwari N, Pataskar A, Peron S, Thakurela S, Sahu SK, Figueres-Onate M, Marichal N, Lopez-Mascaraque L, Tiwari VK, Berninger B (2018) Stage-specific transcription factors drive astrogliogenesis by remodeling gene regulatory landscapes. Cell Stem Cell 23:557–571.e558

Tury A, Mairet-Coello G, DiCicco-Bloom E (2011) The cyclin-dependent kinase inhibitor p57Kip2 regulates cell cycle exit, differentiation, and migration of embryonic cerebral cortical precursors. Cereb Cortex 21:1840–1856

Waclaw RR, Allen 2nd ZJ, Bell SM, Erdelyi F, Szabo G, Potter SS, Campbell K (2006) The zinc finger transcription factor Sp8 regulates the generation and diversity of olfactory bulb interneurons. Neuron 49:503–516

Yang L, Li Z, Liu G, Li X, Yang Z (2022) Developmental origins of human cortical oligodendrocytes and astrocytes. Neurosci Bull 38:47–68

Yang Y, Vidensky S, Jin L, Jie C, Lorenzini I, Frankl M, Rothstein JD (2011) Molecular comparison of GLT1+ and ALDH1L1+ astrocytes in vivo in astroglial reporter mice. Glia 59:200–207

Zheng K, Huang H, Yang J, Qiu M (2022) Origin, molecular specification, and stemness of astrocytes. Dev Neurobiol 82:149–159

Zhou Y, Zhou B, Pache L, Chang M, Khodabakhshi AH, Tanaseichuk O, Benner C, Chanda SK (2019) Metascape provides a biologist-oriented resource for the analysis of systems-level datasets. Nat Commun 10:1523

Zindy F, den Besten W, Chen B, Rehg JE, Latres E, Barbacid M, Pollard JW, Sherr CJ, Cohen PE, Roussel MF (2001) Control of spermatogenesis in mice by the cyclin D-dependent kinase inhibitors p18(Ink4c) and p19(Ink4d). Mol Cell Biol 21:3244–3255

Zindy F, Soares H, Herzog KH, Morgan J, Sherr CJ, Roussel MF (1997) Expression of INK4 inhibitors of cyclin D-dependent kinases during mouse brain development. Cell Growth Differ 8:1139–1150

Acknowledgements

The authors thank Ryoichiro Kageyama, Hiromi Shimojo, Itaru Imayoshi, Fumio Matsuzaki, Daijiro Konno, and Hiroshi Kawasaki for providing research materials; Katsuhiko Ono, Gwanghyun Park, Youngjae Ryu and Sophors Phorl for valuable supports and discussions; and the KBRI Research Equipment Core Facility Team for technical assistance. This study was funded by grants from the KBRI Basic Research Program of the Ministry of Science, ICT, Future Planning (24-BR-01-03, 24-BR-03-01 to YK) and the National Research Foundation of Korea (2022R1A2C1002728 to YK; 2022R1A2C3011663 to TYR).

Author contributions

Wonyoung Lee: Conceptualization; Data curation; Software; Formal analysis; Investigation; Visualization; Methodology; Writing—original draft; Writing—review and editing. **Byunghee Kang**: Data curation; Software; Formal analysis; Writing—original draft. **Hyo-Min Kim**: Data curation; Software; Formal analysis. **Tsuyoshi Ishida**: Investigation. **Minkyung Shin**: Formal analysis; Investigation; Methodology. **Misato Iwashita**: Data curation; Formal analysis; Investigation; Visualization; Methodology. **Masahiro Nitta**: Investigation. **Aki Shiraishi**: Investigation. **Hiroshi Kiyonari**: Investigation. **Koichiro Shimoya**: Investigation. **Kazuto Masamoto**: Formal analysis; Methodology. **Tae-Young Roh**: Supervision; Validation; Investigation. **Yoichi Kosodo**: Conceptualization; Supervision; Funding acquisition; Validation; Investigation; Writing—original draft; Project administration; Writing—review and editing.

Source data underlying figure panels in this paper may have individual authorship assigned. Where available, figure panel/source data authorship is listed in the following database record: biostudies:S-SCDT-10_1038-S44318-024-00325-9.

Disclosure and competing interests statement

The authors declare no competing interests.

Open Access This article is licensed under a Creative Commons Attribution 4.0 International License, which permits use, sharing, adaptation, distribution and reproduction in any medium or format, as long as you give appropriate credit to the original author(s) and the source, provide a link to the Creative Commons licence, and indicate if changes were made. The images or other third party material in this article are included in the article's Creative Commons licence, unless indicated otherwise in a credit line to the material. If material is not included in the article's Creative Commons licence and your intended use is not permitted by statutory regulation or exceeds the permitted use, you will need to obtain permission directly from the copyright holder. To view a copy of this licence, visit http://creativecommons.org/licenses/by/4.0/. Creative Commons Public Domain Dedication waiver http://creativecommons.org/publicdomain/zero/1.0/ applies to the data associated with this article, unless otherwise stated in a credit line to the data, but does not extend to the graphical or creative elements of illustrations, charts, or figures. This waiver removes legal barriers to the re-use and mining of research data. According to standard scholarly practice, it is recommended to provide appropriate citation and attribution whenever technically possible.

© The Author(s) 2024

Expanded View Figures

Figure EV1. The expression level of CDKIs, confirmation of markers, and sample preparation by laser microdissection (LMD).

▶

(**A**) The expression level of CDKIs in RGCs in the developing mouse cortex (reanalysis of La Manno et al, 2021). The dot plot represents the expression level of CDKIs in the population of RGCs from La Manno et al scRNA-seq data. The dot size and color correspond to the proportion of cells that express the gene and the average level (log2-normalized count) of expressing cells. Arrows indicate higher expression at the onset of the gliogenesis stage (around E15-16). (**B**) Confirmation of the specificity of p18 and p27 antibodies. The control vector (a, b, g, h), p18 (c, d, i, j), and p27 (e, f, k, l) were transfected into mouse embryonic fibroblasts (MEFs). Subsequently, immunostaining using p18 (a-f) and p27 (g-l) antibodies was performed on the fixed cells to confirm that there were no cross-reactions between p18 and p27. Bar, 20 µm. (**C**) Sections of the embryonic mouse brains at E14.5 (a–c) and E15.5 (d–f) were immunostained with p18 and PECAM (a marker of a blood vessel) antibodies to confirm that bright dot structures responding to the p18 antibody were blood cells (arrowheads). Bar, 50 µm. (**D**) Confirmation of the specificity of the *Aldh1l1*-EGFP and AldH1l1 antibodies. (a–i) Sections of the *AldH1l1*-EGFP mouse brains at E17.5 (a–c), P0 (d–f), and P10 (g–i) were immunostained with AldH1l1 antibody to confirm that *AldH1l1*-EGFP expression reflects endogenous AldH1l1 protein expression. Bar, 50 µm. (j) Quantification of the immunostaining ($n = 3$ brains each). One-way ANOVA with Tukey's test; error bars show mean ± SEM. No statistically significant differences were detected. (**E**) LMD from mouse brain tissue. (a) Images before and after LMD of freshly frozen mouse brain sections at E13.5–17.5. (b) Quality check of RNA using TapeStation after preparation from mouse brain tissue by LMD (E13.5–17.5).

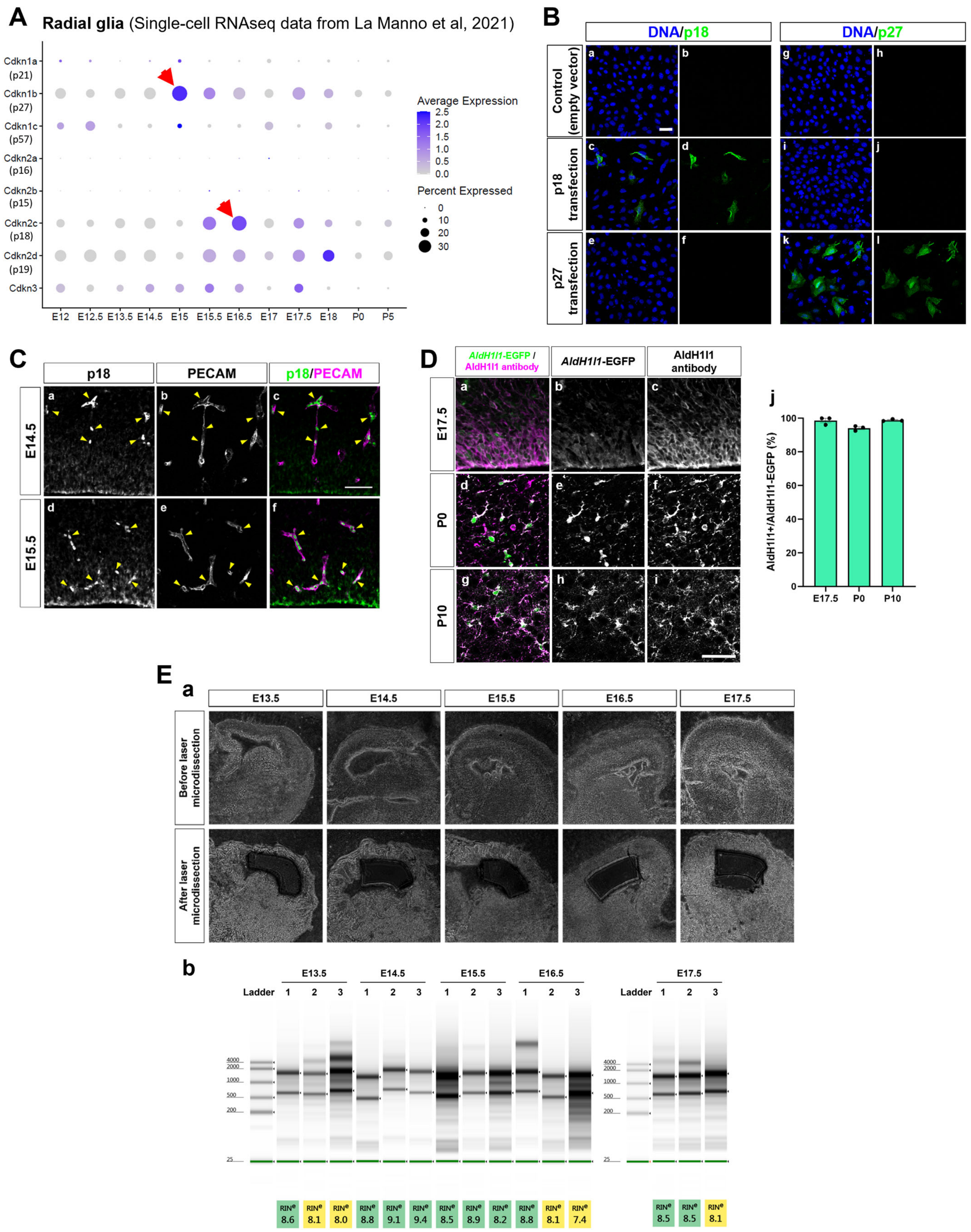
A
Radial glia (Single-cell RNAseq data from La Manno et al, 2021)
Cdkn1a (p21)
Cdkn1b (p27)
Cdkn1c (p57)
Cdkn2a (p16)
Cdkn2b (p15)
Cdkn2c (p18)
Cdkn2d (p19)
Cdkn3
E12 E12.5 E13.5 E14.5 E15 E15.5 E16.5 E17 E17.5 E18 P0 P5
Average Expression
2.5
2.0
1.5
1.0
0.5
0.0
Percent Expressed
0
10
20
30
B
DNA/p18
DNA/p27
Control (empty vector)
p18 transfection
p27 transfection
a b c d e f g h i j k l
C
p18
PECAM
p18/PECAM
E14.5
E15.5
a b c d e f
D
AldH1l1-EGFP / AldH1l1 antibody
AldH1l1-EGFP
AldH1l1 antibody
E17.5
P0
P10
a b c d e f g h i
j
AldH1l1+/AldH1l1-EGFP (%)
0
20
40
60
80
100
E17.5 P0 P10
E
a
E13.5 E14.5 E15.5 E16.5 E17.5
Before laser microdissection
After laser microdissection
b
E13.5 E14.5 E15.5 E16.5 E17.5
Ladder 1 2 3 1 2 3 1 2 3 1 2 3
Ladder 1 2 3
4000
2000
1000
500
200
25
RINe 8.6
RINe 8.1
RINe 8.0
RINe 8.8
RINe 9.1
RINe 9.4
RINe 8.5
RINe 8.9
RINe 8.2
RINe 8.8
RINe 8.1
RINe 7.4
RINe 8.5
RINe 8.5
RINe 8.1

Figure EV2. Characterizations of p18 and p27 OE.

(**A**) Cell cycle inhibition in p18 and p27 OE brains. (a) Plasmids to induce OE of p18 and p27 mixed with pCAG-H2B-EGFP were delivered at E14.5. EdU was administered 2 h before fixation at E15.5. White squares (i-vi) are magnified images of I-III. Arrows; the border between electroporated and nonelectroporated regions. Bars, 200 µm in I-III, and 100 µm in ii, iv, and vi. (b) Quantification of EdU-positive cells among H2B-EGFP-positive cells ($n = 3$ brains each). One-way ANOVA with Tukey's test; error bars show mean ± SEM. From top to bottom, ***$P = 0.00000039$, ***$P = 0.00000120$. (**B**) Distribution of the *AldH1l1*-EGFP-positive cells with p18 OE. (a–d) Plasmids to induce OE of p18 mixed with pCAG-H2B-TagRFP were delivered at E15.5 of the *AldH1l1*-EGFP mice and then fixed at E16.5 (a), 17.5 (b), 18.5 (c), and P0 (d). Positions of the H2B-TagRFP-positive cells from the ventricular surface were measured. The bars indicate the ratio of H2B-TagRFP-positive cells in each zone among all zones ($n = 3$ brains each). Two-tailed t test; error bars show mean ± SEM. From top to bottom, **$P = 0.00160483$ (c), **$P = 0.00782095$, *$P = 0.01564190$ (d). (e) Representative images of the entire span of the dorsal cortex used for the quantification in (d (P0)). The cropped images close to the ventricular surface are presented in the main Fig. 2F (P0). Bar, 50 µm. (**C**) Expressions of astrocyte markers (Sox9 and GFAP) near the ventricular surface by p18 OE. Plasmids to induce OE of p18 mixed with pCAG-H2B-TagRFP were delivered at E15.5 and then fixed at P0. Sections were stained using Sox9 (a) or GFAP (b) antibody. Arrowheads; double-positive cells to Sox9 (a) or GFAP (b) and H2B-TagRFP. Bar, 10 µm. Sox9 (c) or GFAP (d) -positive cells among H2B-TagRFP-positive cells were quantified ($n = 3$ brains). Two-tailed t-test; error bars show mean ± SEM. **$p = 0.00288849$ (c), **$P = 0.00379764$ (d). (**D**) Effects of p18 OE on oligodendrocyte differentiation. (a) Plasmids to induce OE of p18 mixed with pCAG-H2B-TagRFP were delivered at E15.5 of the *AldH1l1*-EGFP mice and then fixed at P0. Sections were stained using PDGFR-alpha and Sox10 antibodies to recognize the oligodendrocyte lineage. Bar, 50 µm. (b) Quantification of Sox10-, PDGFR-alpha-, and *AldH1l1*-EGFP-positive cells among H2B-TagRFP-positive cells ($n = 3$–4 brains each). Two-tailed t test; error bars show mean ± SEM. **$P = 0.00153132$.

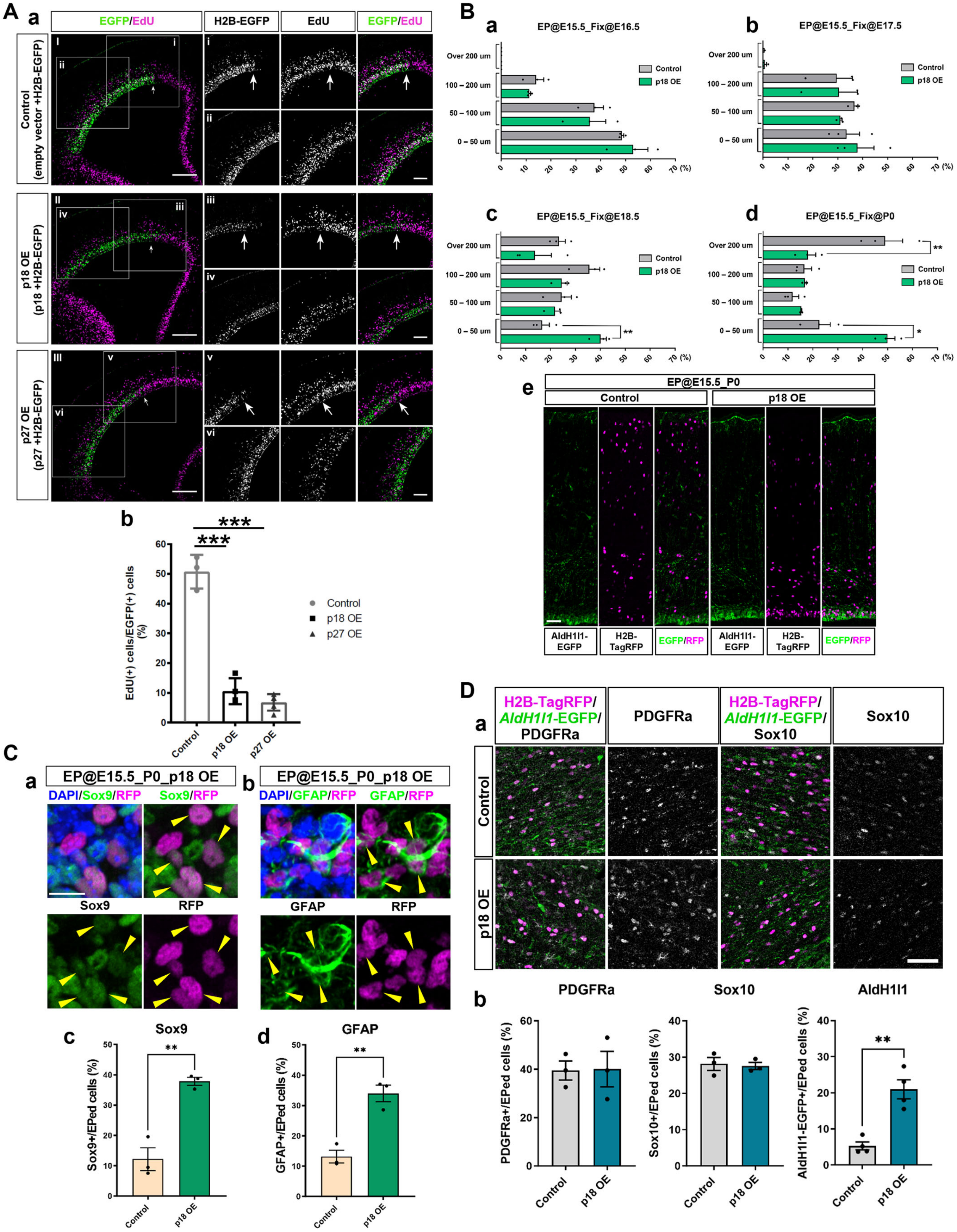
A
a
EGFP/EdU
H2B-EGFP
EdU
EGFP/EdU
Control (empty vector +H2B-EGFP)
p18 OE (p18 +H2B-EGFP)
p27 OE (p27 +H2B-EGFP)
I
II
III
i
ii
iii
iv
v
vi
b
***
***
EdU(+) cells/EGFP(+) cells (%)
0
10
20
30
40
50
60
Control
p18 OE
p27 OE
● Control
■ p18 OE
▲ p27 OE
B
a
EP@E15.5_Fix@E16.5
b
EP@E15.5_Fix@E17.5
c
EP@E15.5_Fix@E18.5
d
EP@E15.5_Fix@P0
Over 200 um
100 – 200 um
50 – 100 um
0 – 50 um
Control
p18 OE
0
10
20
30
40
50
60
70 (%)
**
**
*
e
EP@E15.5_P0
Control
p18 OE
AldH1l1-EGFP
H2B-TagRFP
EGFP/RFP
C
a
EP@E15.5_P0_p18 OE
DAPI/Sox9/RFP
Sox9/RFP
Sox9
RFP
b
EP@E15.5_P0_p18 OE
DAPI/GFAP/RFP
GFAP/RFP
GFAP
RFP
c
Sox9
Sox9+/EPed cells (%)
**
d
GFAP
GFAP+/EPed cells (%)
**
0
10
20
30
40
50
Control
p18 OE
D
a
H2B-TagRFP/AldH1l1-EGFP/PDGFRa
PDGFRa
H2B-TagRFP/AldH1l1-EGFP/Sox10
Sox10
Control
p18 OE
b
PDGFRa
PDGFRa+/EPed cells (%)
0
20
40
60
Sox10
Sox10+/EPed cells (%)
AldH1l1
AldH1l1-EGFP+/EPed cells (%)
0
10
20
30
40
**
Control
p18 OE

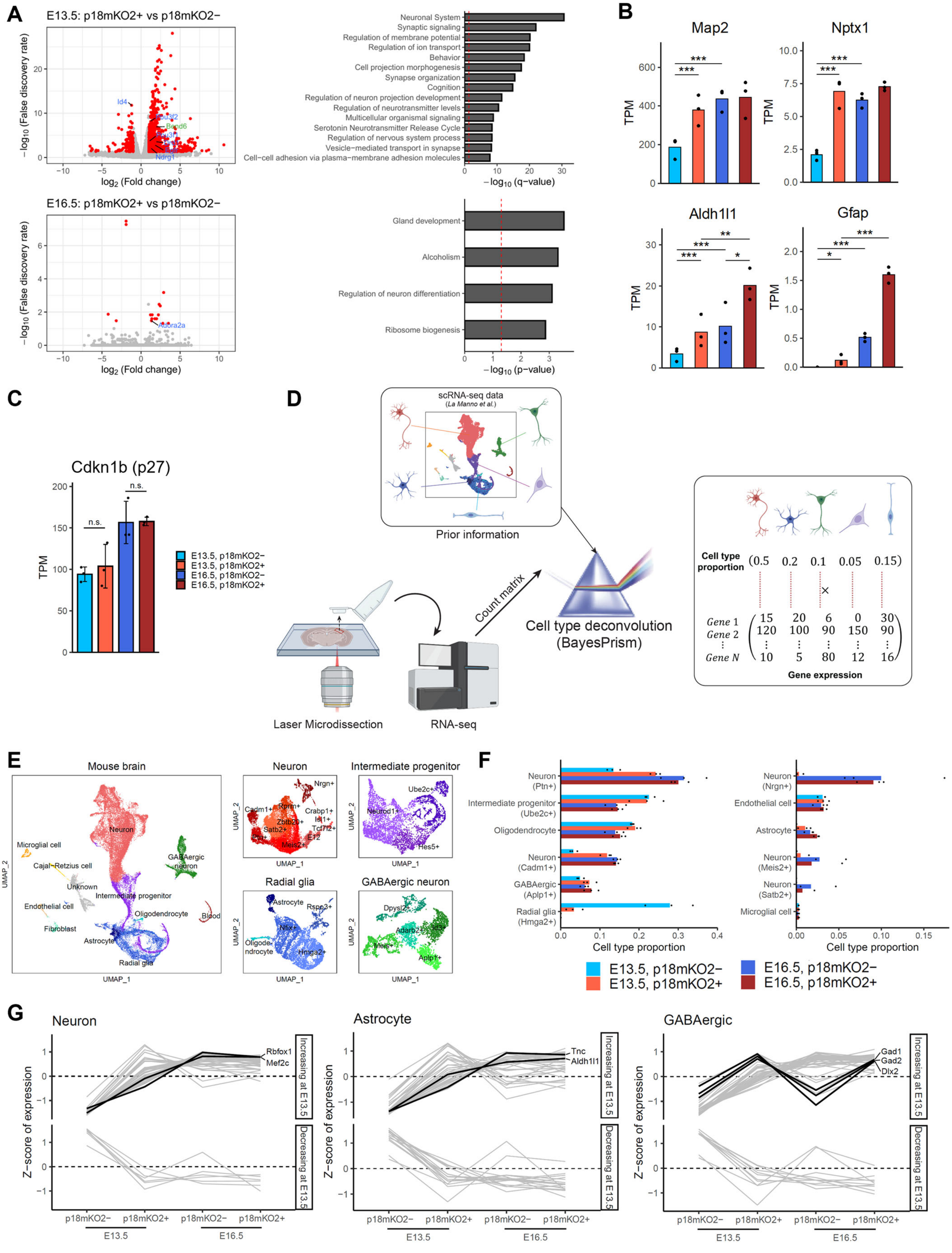
A
E13.5: p18mKO2+ vs p18mKO2−
−log10 (False discovery rate)
log2 (Fold change)
Id4
Pou3f2
Bcan6
Ndrg1
Neuronal System
Synaptic signaling
Regulation of membrane potential
Regulation of ion transport
Behavior
Cell projection morphogenesis
Synapse organization
Cognition
Regulation of neuron projection development
Regulation of neurotransmitter levels
Multicellular organismal signaling
Serotonin Neurotransmitter Release Cycle
Regulation of nervous system process
Vesicle−mediated transport in synapse
Cell−cell adhesion via plasma−membrane adhesion molecules
−log10 (q−value)
E16.5: p18mKO2+ vs p18mKO2−
Adora2a
Gland development
Alcoholism
Regulation of neuron differentiation
Ribosome biogenesis
−log10 (p−value)
B
Map2
Nptx1
Aldh1l1
Gfap
TPM
***
**
*
C
Cdkn1b (p27)
n.s.
TPM
E13.5, p18mKO2−
E13.5, p18mKO2+
E16.5, p18mKO2−
E16.5, p18mKO2+
D
scRNA-seq data
(La Manno et al.)
Prior information
Count matrix
Cell type deconvolution
(BayesPrism)
Laser Microdissection
RNA-seq
Cell type proportion
(0.5 0.2 0.1 0.05 0.15)
Gene 1
Gene 2
Gene N
15 20 6 0 30
120 100 90 150 90
10 5 80 12 16
Gene expression
E
Mouse brain
Neuron
Microglial cell
Cajal−Retzius cell
Unknown
Intermediate progenitor
Endothelial cell
Oligodendrocyte
Fibroblast
Astrocyte
Radial glia
GABAergic neuron
Blood
UMAP_1
UMAP_2
Neuron
Nrgn+
Cadm1+
Rorb+
Crabp1+
Zbtb20+
Isl1+
Satb2+
Tcf7l2+
Ptn+
Meis2+
E12
Intermediate progenitor
Ube2c+
Neurod1+
Hes5+
Radial glia
Astrocyte
Rspo3+
Nfix+
Oligodendrocyte
Hmga2+
GABAergic neuron
Dpysl2+
Adarb2+
Id3+
Meis+
Aplp1+
F
Neuron (Ptn+)
Intermediate progenitor (Ube2c+)
Oligodendrocyte
Neuron (Cadm1+)
GABAergic (Aplp1+)
Radial glia (Hmga2+)
Neuron (Nrgn+)
Endothelial cell
Astrocyte
Neuron (Meis2+)
Neuron (Satb2+)
Microglial cell
Cell type proportion
E13.5, p18mKO2−
E13.5, p18mKO2+
E16.5, p18mKO2−
E16.5, p18mKO2+
G
Neuron
Astrocyte
GABAergic
Z−score of expression
Rbfox1
Mef2c
Tnc
Aldh1l1
Gad1
Gad2
Dlx2
Increasing at E13.5
Decreasing at E13.5
p18mKO2− p18mKO2+ p18mKO2− p18mKO2+
E13.5
E16.5

◀ **Figure EV3. Cell type deconvolution by BayesPrism.**

(**A**) Differential expression analysis comparing mKO2- (Control) and mKO2+ (p18 OE) at each stage. At E13.5 and E16.5, 1,211 and 273 DEGs were identified, respectively. There were changes in the expression levels of genes related to "regulation of neural differentiation" at E13.5, whereas no terms related to brain development were found at E16.5. (**B**) The expression levels of neural markers (*Map2* and *Nptx1*) and astrocyte markers (*Aldh1l1* and *Gfap*) in mKO2- and mKO2+ mice at E13.5 and E16.5. FDR was calculated by DESeq2. From top to bottom, left to right, ***P = = 1.44e-11, ***P = 7.15e-7 (Map2), ***P = 3.63e-11, ***P = 1.28e-10 (Nptx1), **P = 0.000234, ***P = 1.05e-9, ***P = 6.14e-7, *P = 0.00120 (AldH1l1), ***P = 1.36e-5, ***P = 1.58e-5, *P = 0.00936 (Gfap). (**C**) The expression levels of *p27* (*Cdkn1b*) in mKO2- and mKO2+ mice at E13.5 and E16.5 ($n = 3$ for each sample). FDR was calculated by DESeq2; error bars show mean ± SD. No statistically significant differences were detected. (**D**) Schema of the analysis pipeline for the cell type deconvolution. (**E**) UMAPs of scRNA-seq from the developing mouse brain (La Manno et al, 2021). Subtypes of Neuron (*Mapt*+, *Ly6h*+), Intermediate progenitor (*Eomes*+), Radial glia (*Nes*+, *Vim*+) and GABAergic neuron (*Gad1*+, *Gad2*+) were indicated by their marker genes. (**F**) Full deconvolution result using BayesPrism. Each dot represents a replicate of each sample. (**G**) The expression level of the top 50 variable genes found in Fig. 6F at E13.5 and E16.5. Representative genes are indicated by a thick black line.

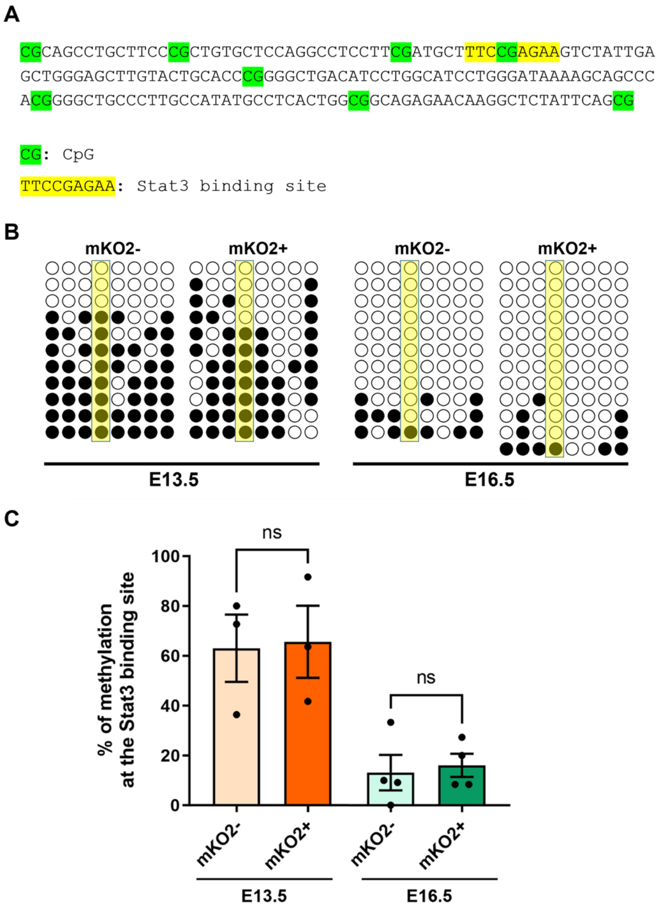

Figure EV4. Bisulfite sequencing analysis to investigate the DNA methylation status.

(**A**) Positions of CpG (green) and the Stat3 binding site at the promoter region of GFAP (yellow) investigated in a previous study (Takizawa et al, 2001). (**B**) Representative results showing methylated sites (black) among CpG positions (circle) in the cortical VZ of p18-P2A-mKO2-negative or -positive mice. Tamoxifen was administered to pregnant R26R-p18-P2A-mKO2/Nes-CreER^{T2} mice at E12.5 and 15.5, and then embryonic brains were dissected at E13.5 and 16.5. After the preparation of fresh brain sections, the genomic DNA from the VZ isolated by LMD was prepared for bisulfite assay. The yellow color indicates the Stat3 binding site. (**C**) Quantification of the methylation status at the Stat3 binding site at E13.5 and E16.5 in mKO2- and mKO2+ mice ($n = 3$ for E13.5 and 4 for E16.5 brains). Two-tailed *t*-test; error bars show mean ± SEM. No statistically significant differences were detected.